UNIVERSITÀ DEGLI STUDI DI MODENA E REGGIO EMILIA

Dipartimento di Scienze Fisiche, Informatiche e Matematiche

Master's Degree Course in

Physics

Analysis of NA62 events with RICH signals off the Cherenkov ring

Thesis Supervisor

Prof. Andrea Bizzeti

Candidate

Ayush

Academic Year 2024–2025

Dedicated to my mother,
for her unwavering support and love.

« *Teachers who make physics boring are criminals.*
» Walter Lewin

Abstract

The Ring-Imaging Cherenkov (RICH) detector of the NA62 experiment is a key component for charged-particle identification, providing precise measurements of particle velocity through the detection of Cherenkov radiation. The performance of the RICH relies on the accurate reconstruction of Cherenkov rings formed by photons reflected by a segmented mirror system and detected on a photon-sensitive plane.

This thesis presents a detailed study of non-ideal RICH hits, referred to as *spurious* hits, which deviate from the expected ring topology and may affect the quality of Cherenkov ring reconstruction. Using reconstructed NA62 data from two different running periods, a robust hit- and event-level classification framework is developed to study the properties of events with and without spurious hits.

The analysis investigates the dependence of spurious-hit behaviour on several event-related parameters, including hit multiplicity and track position on the RICH mirror plane, allowing the identification of possible region-dependent effects. Comparative studies between run periods are performed to assess the stability of the observed features.

The results provide a quantitative characterization of events with different numbers of spurious hits in the NA62 RICH detector.

Acknowledgements

I would like to express my deepest gratitude to my thesis supervisor, **Prof. Andrea Bizzeti**, for his invaluable guidance, constant support, and scientific insight throughout the development of this work. His expertise in experimental particle physics and his active involvement in the NA62 RICH detector group were fundamental in shaping both the direction and the scientific rigor of this thesis. I am especially grateful for his availability, patience, and careful feedback, as well as for providing access to the data sets and analysis tools used in this study and for guiding me through their interpretation.

I would also like to acknowledge the **NA62 Collaboration at CERN**, whose work and publicly documented analysis frameworks form the scientific foundation of this thesis. Although this research was carried out remotely, it benefited greatly from the experimental design, reconstruction software, and analysis strategies developed by the collaboration, in particular for the RICH detector.

I am sincerely grateful to the **Università degli Studi di Modena e Reggio Emilia (UNIMORE)** for providing an excellent academic environment and a solid education in physics. The Master's programme offered by the university equipped me with the theoretical background and analytical tools necessary to engage with a complex experimental analysis connected to a major international collaboration.

Finally, I would like to thank my family and friends for their constant encouragement, patience, and support throughout my studies. Special thanks to **Prof. Walter Lewin** who advised me to take the leap of faith, **Er. Aditya Divyadarshi** who paved the path of my career and **Er. Ratul Suklabaidya** for believing in me. Their trust and motivation have been essential during the most challenging stages of this journey.

Contents

List of Figures

List of Tables

1. Cherenkov Radiation and Cherenkov Detectors

Cherenkov radiation is emitted when a charged particle propagates through a transparent dielectric medium with a velocity exceeding the phase velocity of light in that medium. The phenomenon was first observed experimentally in 1934 by P. A. Cherenkov [1] and was subsequently explained on a firm theoretical basis by Frank and Tamm [2]. Since its discovery, Cherenkov radiation has become a fundamental tool in experimental nuclear and particle physics, particularly for the measurement of particle velocity and for particle identification.

The emission of Cherenkov radiation arises from the coherent electromagnetic response of the medium to the passage of a charged particle moving with velocity $v > c/n$, where n is the refractive index of the medium. The radiation is emitted along the surface of a cone whose opening angle depends on the particle velocity and on the refractive index. By exploiting this geometrical relationship, Cherenkov detectors provide direct access to the kinematic properties of charged particles. Comprehensive discussions of the theoretical foundations and experimental applications of Cherenkov radiation can be found in Refs. [1, 2, 3, 4].

1.1 Physical Origin of Cherenkov Radiation

When a charged particle traverses a dielectric medium, its electric field polarizes the atoms or molecules of the medium. At velocities well below the speed of light in the medium, this polarization follows the particle adiabatically and no radiation is emitted. However, when the particle velocity exceeds the phase velocity of light in the medium, the polarization cannot relax instantaneously, resulting in the emission of electromagnetic radiation.

This radiation originates from the coherent superposition of wavelets emitted by the polarized medium along the particle trajectory. Due to the superluminal motion of the particle, the emitted wavefronts interfere constructively only at a specific angle with respect to the particle direction. The resulting radiation pattern forms a conical wavefront analogous to a

shock wave in acoustics, as illustrated in Fig. 1.

1.1.1 Threshold Condition

Cherenkov radiation is emitted only if the particle velocity exceeds the phase velocity of light in the medium:

$$v > \frac{c}{n}.$$

Expressing the velocity in terms of $\beta = v/c$, the threshold condition becomes

$$\boxed{\beta > \beta_{\text{th}} = \frac{1}{n}}$$

where n is the refractive index of the medium. Below this threshold, no Cherenkov radiation is emitted.

The corresponding momentum can be obtained using the relativistic relations

$$\gamma = \frac{1}{\sqrt{1-\beta^2}}, \qquad p = \gamma m v = \gamma m c \beta.$$

At threshold ($\beta = 1/n$), this leads to

$$\boxed{p_{\text{th}} = \frac{mc}{\sqrt{n^2-1}}}$$

which defines the minimum momentum required for a particle of mass m to emit Cherenkov radiation in a medium with refractive index n.

1.2 Kinematical Description of Cherenkov Radiation

Once the threshold condition is satisfied, Cherenkov radiation is emitted at a fixed angle with respect to the particle trajectory, known as the Cherenkov angle. The geometrical interpretation of Cherenkov radiation, including the emission of a conical wavefront and the definition of the Cherenkov angle, is illustrated in Fig. 1.

The Cherenkov angle θ_c is given by

$$\cos\theta_c = \frac{1}{\beta n}, \tag{1.1}$$

where $\beta = v/c$. For ultra-relativistic particles ($\beta \simeq 1$), the angle approaches a maximum value determined solely by the optical properties of the medium.

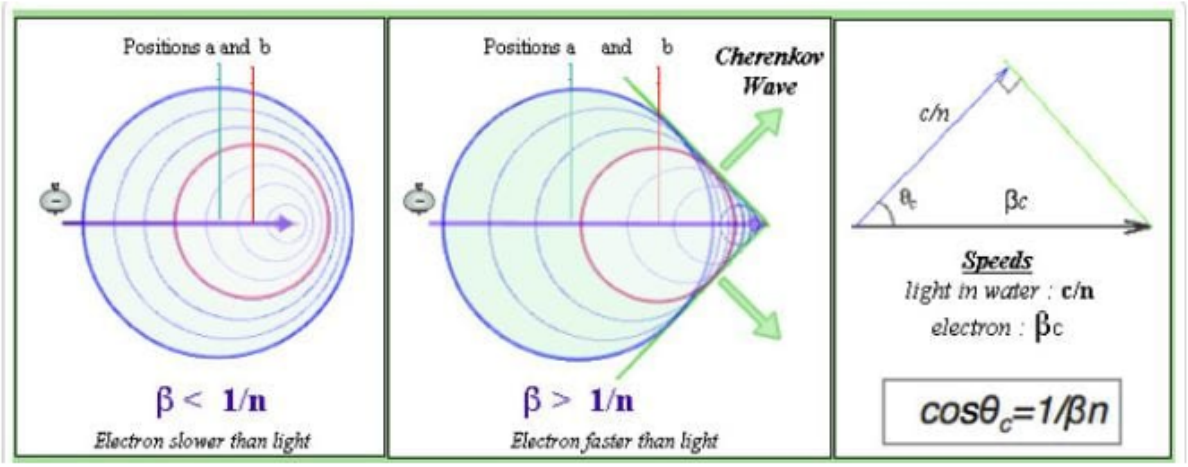

Figure 1: Schematic illustration of Cherenkov radiation in a dielectric medium. (a) A charged particle traveling with velocity below the Cherenkov threshold ($\beta n < 1$) does not produce coherent radiation. (b) When the particle velocity exceeds the phase velocity of light in the medium ($\beta n > 1$), coherent radiation is emitted along a conical wavefront. (c) Geometrical construction defining the Cherenkov angle θ_c, which satisfies $\cos\theta_c = 1/(\beta n)$, where $\beta = v/c$ and n is the refractive index of the medium.

1.2.1 Photon Yield

The number of Cherenkov photons emitted per unit path length and per unit wavelength interval is given by Frank–Tamm formula [2]:

$$\frac{d^2N}{dx\,d\lambda} = \frac{2\pi\alpha}{\lambda^2}\left(1 - \frac{1}{\beta^2 n^2(\lambda)}\right), \tag{1.2}$$

where α is the fine-structure constant and λ is the photon wavelength. The emission spectrum is continuous and strongly weighted toward short wavelengths, a feature that significantly influences detector design.

1.3 Cherenkov Radiation as a Velocity-Sensitive Process

The dependence of the Cherenkov angle on β through relation (1.1) implies that the emission angle provides a direct measurement of the particle velocity, provided that β is above threshold.

In threshold Cherenkov detectors, only the presence or absence of radiation is used to determine whether the particle velocity exceeds β_{th}.

In angle-measuring detectors, such as Ring Imaging Cherenkov detectors, the measured Cherenkov angle allows the determination of β in the region sufficiently above threshold. Close to threshold, the Cherenkov angle becomes very small and the number of emitted photons, which is proportional to $\sin^2\theta_c$, is strongly reduced. The limitation near threshold therefore arises primarily from the low photon yield rather than from the angular variation with velocity.

If the particle momentum is measured independently, for example by a magnetic spectrometer, the combination of p and β allows the particle mass to be determined via relativistic kinematics.

1.4 Cherenkov Detectors

Cherenkov detectors can be classified according to the type of information they provide about the particle velocity. A widely used classification distinguishes between threshold, differential,

and Ring Imaging Cherenkov (RICH) detectors.

1.4.1 Threshold Cherenkov Detectors

Threshold Cherenkov detectors provide a binary response, indicating only whether the particle velocity exceeds the Cherenkov threshold condition $\beta > 1/n$. They are commonly used for particle discrimination over restricted momentum ranges.

1.4.2 Differential Cherenkov Detectors

Differential Cherenkov detectors select particles within a narrow range of velocities by restricting the accepted Cherenkov angles to a limited interval. Since the Cherenkov angle depends explicitly on $\beta = v/c$, a narrow angular acceptance corresponds to a narrow velocity range.

Some differential Cherenkov detectors employ optical focusing elements, such as spherical mirrors, to improve angular resolution. An example is the NA62 KTAG detector, which uses focusing optics to enhance velocity selectivity.

1.4.3 Ring Imaging Cherenkov (RICH) Detectors

Ring Imaging Cherenkov (RICH) detectors measure the Cherenkov angle by reconstructing the pattern produced by Cherenkov photons on a photon detection plane.

Cherenkov photons are emitted along directions forming a fixed angle θ_C with respect to the particle direction of flight. Since the emission occurs continuously along the particle trajectory, the photons illuminate a circular region on a plane approximately perpendicular to the particle direction.

In a RICH detector, a spherical mirror is used to reflect and focus the Cherenkov photons onto the photon detection plane. This optical focusing converts the circular illumination into a ring-shaped pattern on the focal plane.

The radius of the reconstructed ring is directly related to the Cherenkov angle θ_C, and therefore to the particle velocity through Eq. (1.1). By measuring the ring radius, RICH detectors provide a precise determination of the particle velocity above threshold.

2. The NA62 Experiment and its RICH Detector

2.1 Overview of the NA62 Detector Setup

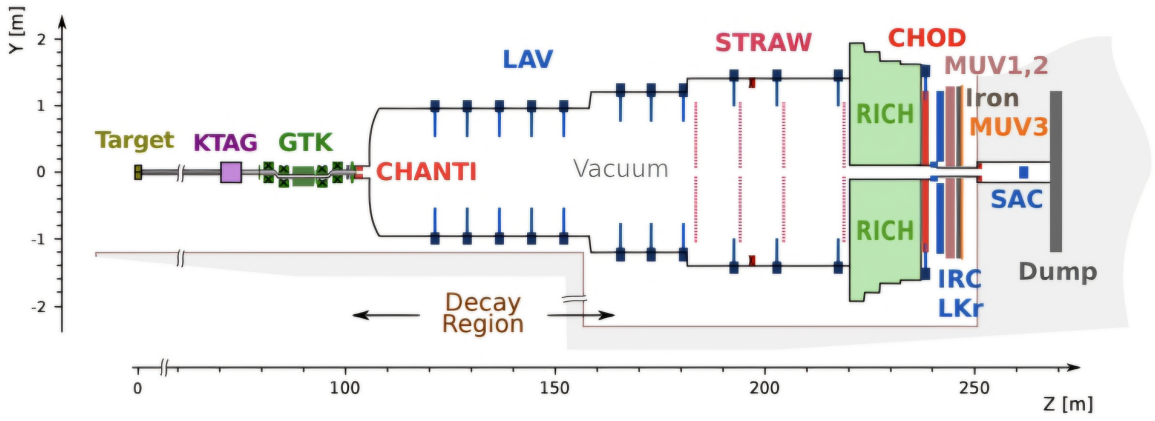

Figure 2: Schematic layout of the NA62 detector setup highlighting the main subdetectors along the beam line.

A detailed description of the NA62 beam line and detector systems can be found in Ref. [5].

A schematic overview of the NA62 detector layout is shown in Fig. 2, highlighting the main subdetectors arranged along the beam line. The NA62 experiment at CERN is designed to study rare kaon decays, with particular emphasis on the ultra–rare process $K^+ \to \pi^+ \nu\bar{\nu}$. Achieving this goal requires precise tracking, excellent time resolution, and highly efficient particle identification across a wide momentum range.

The beam line is the evacuated region along which the secondary hadron beam travels from the production point to the downstream detectors. It begins at the kaon production target, where 400 GeV/c protons from the CERN SPS strike a fixed target, producing a secondary beam composed primarily of pions, protons, and kaons. Upstream kaon identification is provided by the KTAG detector, a differential Cherenkov counter capable of tagging beam kaons

with a time resolution of about 100 ps. The beam spectrometer (GTK), located upstream of the decay region, measures the momentum, direction, and time of individual beam particles before they enter the decay region. The decay region is a long, evacuated volume in which kaons are allowed to decay in flight, minimizing interactions with detector material. Downstream detectors are positioned after the decay region and are responsible for reconstructing the charged and neutral decay products, providing tracking, calorimetry, timing, and particle-identification information.

The beam line defines the longitudinal Z axis, with its origin at the kaon production target and the positive direction corresponding to the downstream beam direction. The vertical direction defines the Y axis, while the horizontal direction defines the X axis, forming a right–handed coordinate system. This coordinate convention is used consistently throughout the experiment for detector alignment, tracking, and reconstruction.

To minimize interactions of beam particles with detector material, the beam spectrometer, the decay region, and most downstream detectors are placed in vacuum. This design choice reduces multiple scattering and improves the resolution of kinematic measurements. Precise time matching between a beam kaon measured upstream and charged decay products reconstructed downstream is essential and must be controlled at the level of 100–150 ps in order to maintain a correct association probability exceeding 99%.

2.1.1 High-Intensity Kaon Beam Line

The primary proton beam is extracted from the CERN SPS accelerator at a momentum of 400 GeV/c and directed onto a beryllium target (T10), 400 mm in length and 2 mm in diameter.Secondary particles of different types and electric charges are produced at the target. A positively charged hadron beam with central momentum 75 GeV/c is selected using magnetic elements and collimators. The kaon component is about 6%, the remainder being mainly pions and protons.

A system of four dipole magnets arranged in an achromat configuration performs both momentum selection and beam transport. Collimators placed along the beam line absorb unwanted particles and define the transverse acceptance. Additional magnetic elements are used to sweep away muons and other background particles, ensuring that a well-defined hadron beam with a controlled kaon component enters the decay region.

2.1.2 Kaon Identification: KTAG

Kaon identification in the beam is provided by a differential Cherenkov detector equipped with a dedicated photon detection system known as KTAG, illustrated in Fig. 3. Kaons constitute only a small fraction of the secondary hadron beam, and their identification is essential for associating downstream decay products with the correct beam particle.

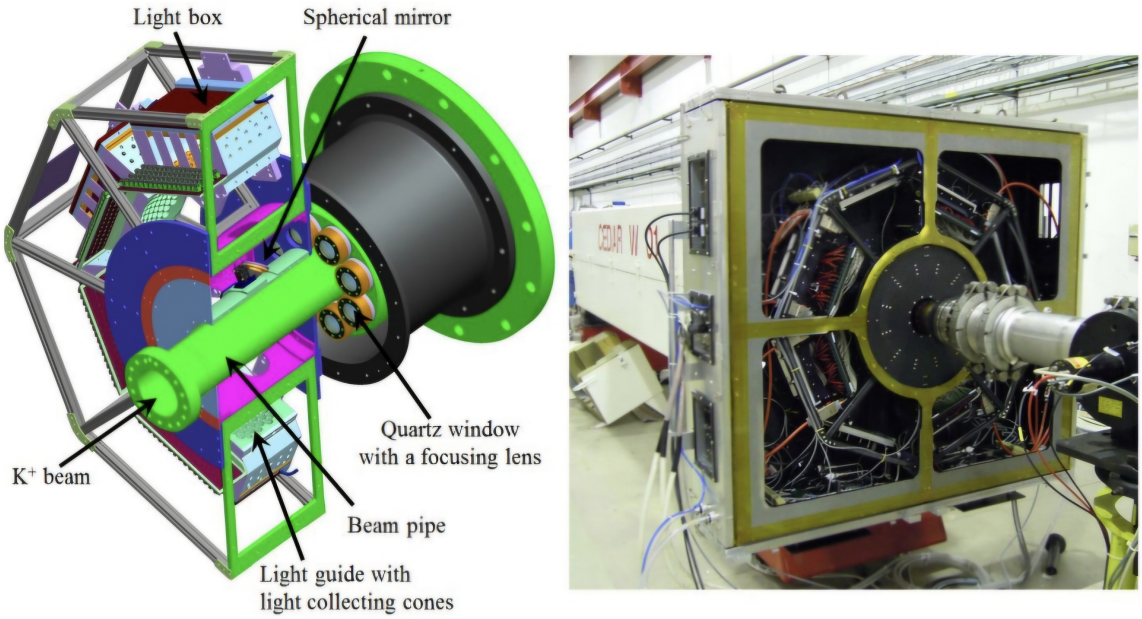

Figure 3: Left: Drawing of the upstream part of the KTAG detector. Right: KTAG installed in the NA62 beam line during a test run in 2012, with four of the eight sectors equipped.

Cherenkov light produced in the gaseous radiator is reflected by spherical mirrors and focused onto an annular diaphragm ("ring image"), which selects photons corresponding to the kaon Cherenkov angle. Only particles producing light at the correct angle pass through the diaphragm and are detected by photomultipliers arranged in eight sectors. The KTAG system provides a time resolution of approximately 100 ps, enabling precise kaon tagging even at high beam rates.

2.1.3 Beam Spectrometer: GTK

The Gigatracker (GTK) measures the momentum and direction of all beam particles; it does not distinguish kaons from pions or protons. The beam spectrometer consisting of three silicon pixel stations is installed inside the vacuum beam pipe. These stations are arranged around a second achromat composed of dipole magnets, which introduces a mo-

mentum–dependent vertical displacement of the beam between the second and third magnet, illustrated in Fig. 4.

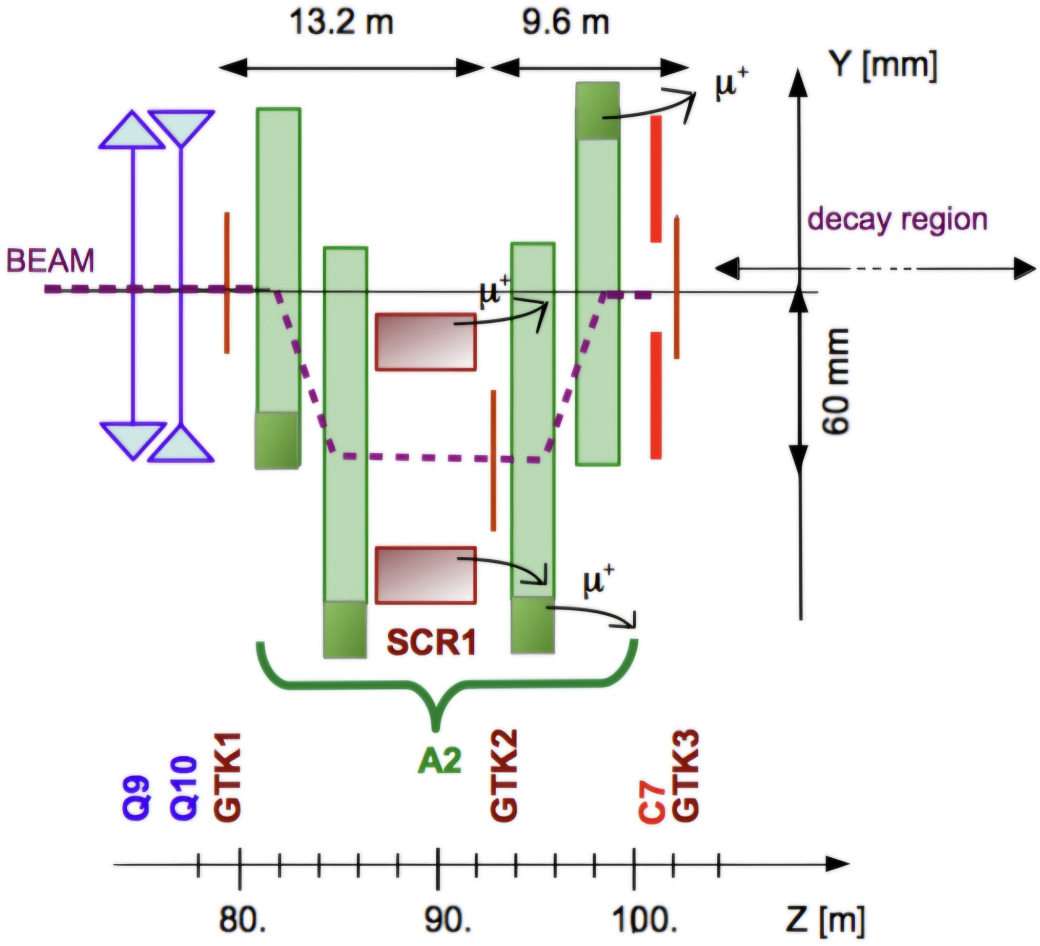

Figure 4: Schematic layout of the beam tracking and momentum measurement in the second achromat. The beam is deflected vertically by 60 mm and returned to its nominal direction after the momentum measurement. Muons are swept away by the scraper SCR1 and the return yokes of the last two C-shaped magnets of the achromat (dark shaded areas).

The GTK measures the kaon momentum with a relative precision of about 0.2% and determines the particle direction with an angular resolution of approximately 16 μrad. Due to the extremely high beam rate, the detector must also provide a time resolution better than 200 ps. The low material budget of each station minimizes multiple scattering and reduces background from inelastic interactions.

2.1.4 Charged Anti-Coincidence Detector: CHANTI

The CHANTI detector is located immediately downstream of the last GTK station and serves to identify inelastic interactions of beam particles with the tracker material. It is equipped with two readout planes, with the scintillator bars oriented vertically and horizontally to form X and Y views.

CHANTI consists of six scintillator stations arranged around the beam line, each equipped with horizontal and vertical readout planes. Charged particles traversing the scintillator produce light that is collected by wavelength–shifting fibres and detected by silicon photomultipliers. Signals in CHANTI are used to veto events associated with upstream interactions.

2.1.5 Decay Region and Photon Veto System

The decay region is contained within a long evacuated tank downstream of the beam spectrometer, starting just after the CHANTI detector. Surrounding this region is a system of photon veto detectors designed to provide hermetic coverage for photons emitted in kaon decays.

Large-Angle Veto (LAV) detectors are positioned along the vacuum vessel to detect photons emitted at angles up to approximately 50 mrad. At smaller angles, photons are intercepted by the Liquid Krypton electromagnetic calorimeter (LKr), as well as the Intermediate-Ring Calorimeter (IRC) and the Small-Angle Calorimeter (SAC). Together, these detectors provide the high photon rejection efficiency required to suppress backgrounds from kaon decays involving neutral pions.

2.1.6 Straw Spectrometer

Downstream of the decay region, the straw spectrometer measures the trajectories(tracks) and momenta of charged particles produced in kaon decays. It extends over a length of approximately 35 m along the beam line and consists of four straw tracking chambers installed inside the vacuum tank, together with a large–aperture dipole magnet (MNP33).

The dipole magnet provides an integrated magnetic field of about 0.9 Tm, corresponding to a transverse momentum kick of approximately 270 MeV/c in the horizontal plane. The spectrometer is designed using light materials and operates in vacuum in order to minimize multiple scattering. The total material budget corresponds to about 1.8% of a radiation

length.

The resulting momentum resolution of the spectrometer is

$$\frac{\sigma(p)}{p} = 0.30\% \oplus 0.005\% \cdot p, \tag{2.1}$$

where the momentum p is expressed in GeV/c. The track angular resolution decreases from about 60 μrad at 10 GeV/c to approximately 20 μrad at 50 GeV/c. These performance figures satisfy the requirements for precise reconstruction of charged decay products in the NA62 experiment.

2.1.7 Ring Imaging Cherenkov Detector

The Ring Imaging Cherenkov (RICH) detector is located downstream of the straw spectrometer and provides charged particle identification as well as precise timing information. The detector consists of a 17 m long radiator volume filled with neon gas at atmospheric pressure.

Charged particles traversing the radiator emit Cherenkov photons, which are reflected by a system of spherical mirrors onto a photon–sensitive detection plane. The radius of the resulting ring is directly related to the velocity of the particle, which, together with the measured momentum, enables the separation of electrons, muons, pions, and kaons over a wide momentum range.

In addition to particle identification, the RICH detector provides a time resolution of the order of 100 ps, contributing to the global event timing and improving the matching between upstream(beam) and downstream detectors. A detailed description of the RICH detector design, reconstruction, and performance is presented in the following section 2.2.

2.1.8 Downstream Timing and Muon Veto Detectors

Immediately downstream of the RICH detector is the Charged Hodoscope (CHOD), composed of scintillator slabs and tiles. CHOD provides fast timing signals with a resolution of approximately 150 ps and is used to define the reference trigger time.

Muon identification is performed by a system consisting of two detectors (MUV1 and MUV2) forming a hadron calorimeter followed by a plane of scintillator tiles (MUV3) placed behind

a an 80 cm thick iron absorber. This system distinguishes muons from pions based on their penetration depth and energy deposition.

Additional detectors placed at strategic locations ensure hermetic coverage for charged particles produced in multi–track kaon decays, further improving background rejection.

2.2 The Ring Imaging Cherenkov Detector (RICH)

The Ring Imaging Cherenkov (RICH) detector is designed to separate pions from muons in the momentum range between 15 and 35 GeV/c, provide a muon suppression factor of at least 100. This performance is a key contribution to the overall background rejection required by the NA62 experiment.

To ensure full detection efficiency for 15 GeV/c pions, the Cherenkov threshold must be sufficiently below this value and not too close to it. While this condition would also be satisfied by any lower threshold, the separation power between pions and muons up to 35 GeV/c requires keeping the momentum threshold as high as possible.

This is because the dependence of the Cherenkov angle on momentum is strongest near threshold and decreases with increasing momentum (see Fig. 7, right). A threshold of approximately 12.5 GeV/c represents a suitable compromise: the average number of detected pion hits at 15–16 GeV/c ($\langle N_{\text{hits}}(\pi)\rangle \approx 7.5$) is still acceptable (see Fig. 7, left), while good π/μ separation is maintained up to 35 GeV/c.

The corresponding refractive index is

$$n \simeq 1.000062,$$

which matches the refractive index of neon gas at atmospheric pressure and room temperature.

For ultra-relativistic particles ($\beta = 1$), the maximum Cherenkov angle is given by

$$\cos\theta_C^{\max} = \frac{1}{n},$$

which yields

$$\theta_C^{\max} \approx 11.2 \text{ mrad}.$$

In addition to particle identification, the RICH provides precise timing information. The pion crossing time is measured with a resolution of about 100 ps, allowing the RICH to serve as a reference timing detector for charged tracks.

2.2.1 The Radiator Vessel

A schematic view of the NA62 RICH detector and its radiator vessel is shown in Fig. 5.

The Cherenkov radiator medium is neon gas, operated at approximately atmospheric pressure. Charged particles traversing the neon emit Cherenkov photons when their velocity exceeds the Cherenkov threshold, producing the light detected by the RICH photomultiplier array.

The radiator vessel is a cylindrical structure 17.5 m long, constructed from ferro–pearlitic steel and filled with neon gas. The vessel is composed of four longitudinal sections with gradually decreasing diameters along the beam direction. At the upstream end, the internal diameter is approximately 3.8 m, while at the downstream end — where the mirror system is installed — the diameter reduces to about 3.2 m.

The inner surfaces of the vessel are coated with black epoxy paint in order to suppress unwanted reflections and minimize background light contributions.

The radiator volume is evacuated before filling with neon gas. During operation, the gas pressure is maintained at approximately 990 mbar in a sealed configuration, ensuring stable gas density and refractive index. The detector is largely insensitive to common impurities such as oxygen and water vapor due to its photon detection threshold above 190 nm.

The refractive index of the gas depends on the neon density according to

$$n = 1 + (n_0 - 1)\frac{\rho}{\rho_0}, \tag{2.2}$$

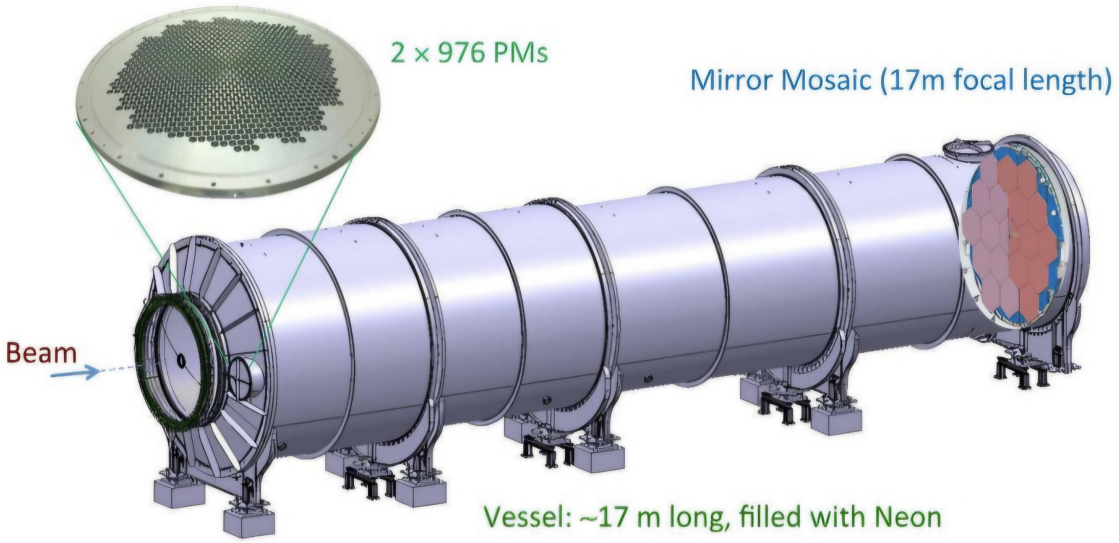

Figure 5: Schematic view of the RICH detector: The hadron beam enters from the left and travels throughout the length of the detector in an evacuated beam pipe. A zoom on one of the two disks accommodating the light sensors (PMs) is shown on the left; the mirror mosaic is made visible through the neon container (vessel) on the right.

where n_0 and ρ_0 are the refractive index and density at normal temperature and pressure.

2.2.2 The Mirror System

The RICH mirror system and its alignment mechanism are shown in Fig. 6. Cherenkov light produced in the radiator is reflected by a mosaic of spherical mirrors arranged at the downstream end of the vessel. The mirrors have a nominal radius of curvature of 34 m, corresponding to a focal length of 17 m, providing a total reflective surface exceeding 6 m^2. The mirror mosaic at the downstream end of the RICH contains 18 hexagonal (350 mm side) and two semi-hexagonal mirrors (adjacent to the beam pipe opening).

To avoid absorption of reflected Cherenkov light by the beam pipe, the mirror mosaic is divided into two spherical surfaces, named Jura and Salève, one with the centre of curvature located to the left and one to the right of the beam pipe.

The mirrors are mounted on a lightweight aluminum honeycomb support structure to ensure mechanical stability while minimizing additional material along the path of charged particles propagating downstream toward detectors such as CHOD and LKr. Each mirror is equipped with piezoelectric actuators that allow remote, fine alignment in two angular directions. The mirror alignment was initially performed using laser measurements and later verified with

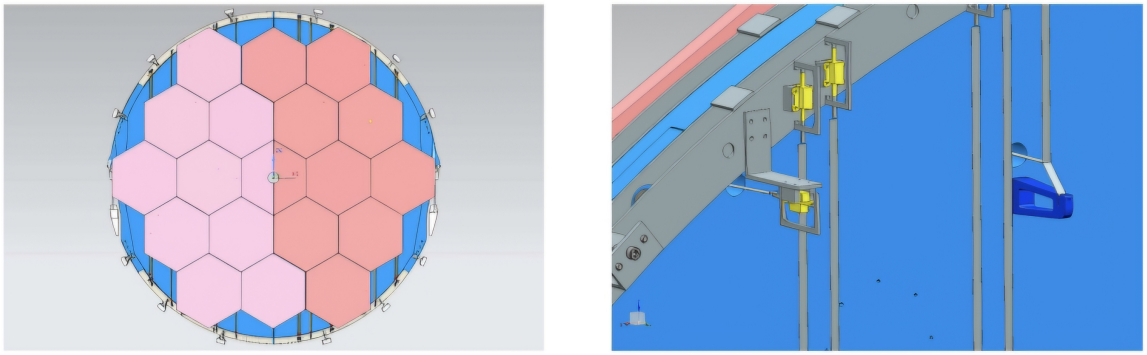

Figure 6: Left: The mirror mosaic at the downstream end of the RICH. Different colours indicate mirrors belonging to the two spherical surfaces, named Jura and Salève sides. Right: Sketch of the mirror alignment system. Three piezoelectric motors (yellow boxes) can be seen; the leftmost motor is pulling the mirror directly; on the right a transmission tool (blue object) changes the ribbon direction from vertical to horizontal.

beam data by selecting tracks whose Cherenkov photons were fully contained within the area of a single mirror, allowing the alignment of that mirror to be checked independently.

2.2.3 The Photon Detection System

Cherenkov photons are detected by an array of photomultiplier tubes (PMTs) arranged on two regions located at the focal surfaces of the mirrors, each plane collecting the light reflected by half of the mirrors. The photon detection system consists of 1952 photomultiplier tubes, arranged in two regions corresponding to the two mirror spherical surfaces (Jura and Salève). The photomultipliers are installed with a pitch of 18 mm, ensuring sufficient angular resolution for Cherenkov ring reconstruction.

The photodetectors are Hamamatsu R7400 U-03 photomultipliers, selected for their fast response, compact dimensions, and reasonable cost. Photomultipliers have a cylindrical shape with a 16 mm wide base and an active area of 8 mm diameter. The sensitivity starts at a wavelength of 185 nm and peaks at 420 nm.

Each photomultiplier is coupled to a Winston cone light-collection system. The Winston cones have the shape of truncated circular paraboloids and are covered with highly reflective aluminized Mylar foil. They are 21.5 mm high, with an entrance aperture of 18 mm and an exit aperture of 7.5 mm, increasing the geometrical acceptance and reducing dead space between adjacent channels.

The photomultipliers are operated at a gain of approximately 1.5×10^6. The single–photoelectron

transit-time spread is about 280 ps. When several photons are detected per ring, this results in a track time resolution of about 70–80 ps.

The photomultiplier signals are processed by fast discriminator electronics based on the NINO ASIC and digitized by high-resolution time-to-digital converters. Both leading and trailing edges are recorded, allowing offline corrections for time slewing effects.

2.3 RICH Ring Geometry and Merged PMT Reference Frame

2.3.1 Merged PMT Reference Frame

For each PMT region (Jura and Salève), a local two–dimensional coordinate system (x, y) is defined. The origin of each local system corresponds to the position where a Cherenkov photon travelling parallel to the beam axis For each PMT region (Jura and Salève), a local two–dimensional ($\frac{dx}{dz} = 0$ and $\frac{dy}{dz} = 0$) and reflected on a mirror on the same side (Jura and Salève) would be detected.

The positions of the origins of the two local coordinate systems are determined through dedicated calibration procedures.

A merged photomultiplier plane is defined by superposing the two PMT regions, with their local origins positioned at the same point.

In this merged PMT reference frame, each (x, y) coordinate corresponds uniquely to a photon direction $(dx/dz, dy/dz)$ before reflection, independently of the photomultiplier region where the photon was detected.

2.3.2 Ring and Hit Geometry

In the merged PMT reference frame, each detected photon hit is described by the coordinates (x_i, y_i) of the centre of the corresponding PMT.

The reconstructed ring centre (x_c, y_c) is determined from the fit to the spatial distribution of detected photon hits and corresponds to the direction of the charged particle trajectory.

For a given Cherenkov angle θ_C and focal length f of the mirror system, the expected ring radius is

$$R = f \tan\theta_C \simeq f\,\theta_C, \tag{2.3}$$

where the small-angle approximation is used, since $\theta_C < 12$ mrad in the NA62 RICH.

2.3.3 Performance

The RICH detector was installed and commissioned in 2014 and has operated successfully during subsequent data–taking periods. The intrinsic event time resolution is approximately 70 ps, while the combined time resolution relative to the KTAG is about 140 ps.

The performance of the RICH detector is illustrated in Fig. 7.

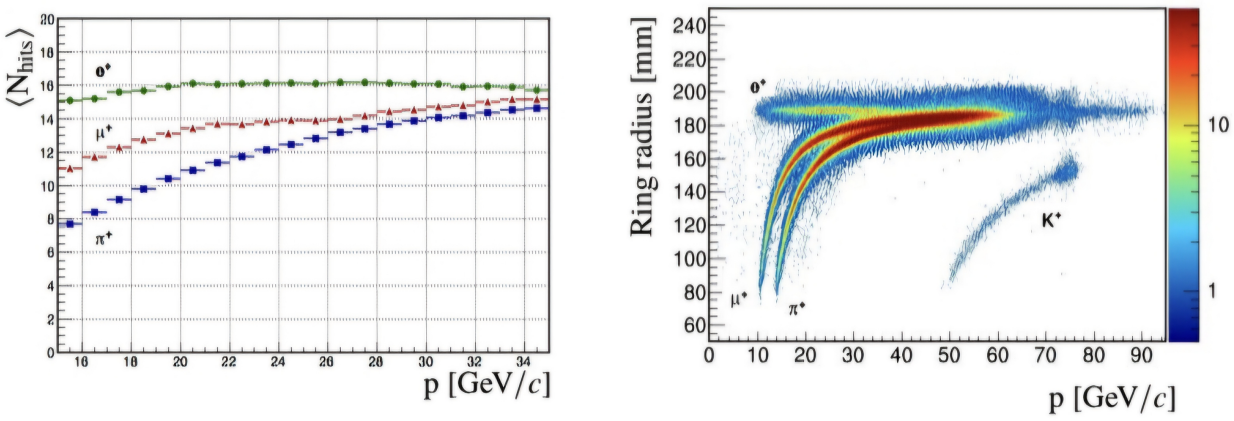

Figure 7: Left: Number of hits per Cherenkov ring vs. particle momentum; electrons, muons and charged pions were selected using spectrometer and calorimetric information. Right: Cherenkov ring radius vs. particle momentum; electrons, muons, charged pions and scattered beam kaons can be seen. Particles with momentum higher than 75 GeV/c are muons from the beam halo.

Distinct particle bands corresponding to electrons, muons, and charged pions are visible over most of the momentum range, enabling efficient π–μ separation in the 15–35 GeV/c region.

3. Event Selection and RICH Data Analysis Framework

This chapter describes the chain of operations that transforms raw NA62 detector signals into the selected event sample used for the spurious–hit analysis in the RICH detector.

In the NA62 reconstruction framework, a *track* is the reconstructed trajectory of a charged particle measured in the straw spectrometer. The spectrometer consists of four straw tracking chambers and a dipole magnet providing a transverse momentum kick. The positions measured in the straw chambers are used to reconstruct the particle trajectory, while the deflection of the track in the magnetic field allows the particle momentum to be determined.

The chapter is organised in three logically distinct parts:

1. The NA62 trigger and data acquisition system.
2. The Ke3 event pre-selection applied at CERN to produce the input ROOT files.
3. The event selection implemented in the RICHAnalysis framework.
4. The hit and event classification.

The RICHAnalysis framework is a dedicated analysis software developed to process reconstructed NA62 events stored in ROOT files. ROOT is a data-analysis framework widely used in high-energy physics, providing efficient storage and processing of large datasets. A ROOT file contains event-based data structures (`TTrees`) that store reconstructed quantities from the different NA62 subdetectors. Within this framework, the relevant detector information is extracted and additional selections are applied.

Particular care is taken to distinguish between selections performed at CERN during data processing and those applied specifically for this analysis.

3.1 NA62 Trigger and Data Acquisition

The large rate of kaon decays occurring in the NA62 decay region produces a high rate of detector signals and therefore requires a high-performance Trigger and Data Acquisition (TDAQ) system capable of reducing the event rate while preserving efficiency for rare kaon decays. To meet these requirements, NA62 employs a unified trigger and readout architecture consisting of a hardware Level–0 (L0) trigger followed by a software Level–1 (L1) trigger. [6]

3.1.1 Level–0 Hardware Trigger

The Level–0 (L0) trigger is the first stage of the NA62 trigger system and is implemented in hardware. It processes fast logical signals ("trigger primitives") produced by several NA62 subdetectors, including the RICH, CHOD, LKr, LAV and MUV3 detectors.

These primitives are transmitted to the Level–0 Trigger Processor, where they are combined to form several independent trigger conditions, referred to as *L0 trigger lines* in NA62 terminology.

The L0 trigger is designed to operate at very high rates, with a maximum output rate of about 1 MHz and a maximum latency of 1 ms.

Each L0 trigger line corresponds to a different combination of detector primitives, designed to select specific physics topologies or to provide control samples for detector studies.

3.1.2 Level–1 Software Trigger

The Level–1 (L1) trigger is a software-based trigger stage executed on the NA62 computing farm. It processes the detector data of each event accepted by the L0 trigger and performs a fast event reconstruction using simplified versions of the offline reconstruction algorithms.

Several independent L1 trigger lines are implemented, each corresponding to a different physics selection strategy. The L1 trigger further reduces the event rate by about one order of magnitude, from approximately 1 MHz at the L0 output to about 100 kHz.

Events accepted by the L1 trigger are written to permanent storage and subsequently processed by the full NA62 offline reconstruction chain.

3.1.3 Control Trigger

In addition to physics trigger lines, NA62 operates a minimum-bias trigger referred to as the *Control trigger*. This trigger is based on signals from the CHOD detector and is recorded with a large downscaling factor of about 400.

The Control trigger does not apply specific physics selections and therefore provides an unbiased sample of events. It is primarily used to determine the K^+ flux, measure detector efficiencies and estimate backgrounds.

The data sample analysed in this thesis is collected using the Control trigger and subsequently processed by the standard NA62 offline reconstruction chain.

3.2 From Data Acquisition to Offline ROOT Samples

The events accepted by the NA62 trigger system, described in Section 3.1, are recorded in raw data format and subsequently processed by the standard NA62 offline reconstruction chain.

The offline reconstruction transforms digitised detector signals into fully reconstructed physics objects, including charged tracks (detected with the STRAW spectrometer), energy clusters in the LKr calorimeter, and RICH rings. The output of this chain is stored in ROOT files with a structured, event-based format that provides a uniform interface for physics analyses.

3.3 Ke3 Pre-selection at CERN

The input to the RICHAnalysis framework consists of ROOT files produced at CERN after a dedicated pre-selection of $K^+ \to \pi^0 e^+ \nu$ (Ke3) events within the standard NA62 offline reconstruction chain. This pre-selection is implemented through the official `ke3` preselection filter and ensures that the input data sample is already enriched in well-reconstructed $K^+ \to \pi^0 e^+ \nu$ decays before any dedicated RICH analysis is performed.

An event must satisfy the following requirements:

1. **Single charged track:** Exactly one reconstructed charged track is required. The track must satisfy the following criteria:
    - Positive electric charge;

- Geometrical acceptance within the CHOD, all STRAW stations, and the LKr calorimeter;
- A reconstructed vertex with the beam axis located within the decay region ($110 < z < 180$ m);
- Good track-fit and vertex quality ($\chi^2_{\text{vertex}} < 20$ and CDA < 25 mm);
- Track momentum in the range $5 < p < 50$ GeV/c.

Here, CDA (Closest Distance of Approach) denotes the minimum distance between the reconstructed charged-particle trajectory and the nominal beam axis.

2. **No additional activity:** no other reconstructed tracks are allowed within 10 ns of the selected track.
3. **Muon rejection:** no hits in the MUV3 detector associated with the selected track.
4. **Two gamma photons:** exactly two LKr energy clusters are required, satisfying:
   - energy $E > 2$ GeV;
   - time within 6 ns of the selected track;
   - distance of at least 150 mm from the track impact point on the LKr.
5. π^0 **consistency:** The two LKr clusters must be kinematically consistent with a $\pi^0 \to \gamma\gamma$ decay originating from the reconstructed vertex position.
6. **Kinematic constraints:** The total reconstructed momentum of the system (track plus two photons) must satisfy 15 GeV/$c < p_{\text{tot}} < 70$ GeV/c, and the total transverse momentum (the component of the total momentum orthogonal to the beam direction) must lie in the range 40 MeV/$c < p_T < 250$ MeV/c, ensuring consistency with the presence of an undetected neutrino.

In addition, particle-identification and background-rejection criteria are applied.
The ratio between the energy deposited by the charged particle in the LKr calorimeter and the momentum of the charged particle measured by the magnetic spectrometer, E_{LKr}/p, is required to satisfy $0.96 < E_{\text{LKr}}/p < 1.03$, ensuring compatibility with the positron hypothesis.

Furthermore, the event must be inconsistent with the $K^+ \to \pi^+\pi^0$ decay mode. This is achieved by requiring that the squared missing mass, computed from the average beam kaon and the reconstructed charged track, satisfies the corresponding selection criteria:

$$m^2_{\text{miss}} = \frac{1}{c^2}\,|P_K - P_\pi|^2 > 0.04\ \text{GeV}^2/c^4 \quad \text{or} \quad m^2_{\text{miss}} < 0.$$

Here:

- P_K is the four-momentum of an *average beam kaon*, defined as a K^+ particle moving along the nominal beam axis with momentum equal to the average beam momentum;
- P_π is the reconstructed four-momentum of the charged track, computed under the pion mass hypothesis using the STRAW spectrometer measurement of the charged particle three-momentum $\vec{p}$.

For genuine $K^+ \to \pi^+\pi^0$ decays, m^2_{miss} peaks at the squared neutral pion mass, $m^2_{\pi^0} \simeq 0.018\ \text{GeV}^2/c^4$. The above requirement therefore suppresses this background by rejecting events in the kinematic region around the $K^+ \to \pi^+\pi^0$ peak.

The events satisfying all the above criteria are written to ROOT files. These filtered samples constitute the input to the dedicated RICHAnalysis framework described in the following sections.

3.3.1 Structure of the RICHAnalysis Input ROOT Files

Each RICHANALYSIS input ROOT file contains a central `TTree` structure in which every entry corresponds to one triggered and reconstructed event. The event record includes dedicated branches for the reconstructed information from the main NA62 subdetectors, in particular:

- STRAW spectrometer tracks, providing momentum components, vertex position and track time;
- RICH reconstructed rings, including centre coordinates (x_c, y_c), ring radius R and ring time t_{ring}; photon hits, including hit positions (x_i, y_i) and hit times t_{hit}.
- LKr calorimeter clusters, with reconstructed energy, position and time;
- global timing references, such as the RICH reference time t_{RICH} and the trigger time t_{trigger}.
- calorimetric particle-identification variables (`CalProbElectron`, `CalProbPion`);

- the energy-over-momentum ratio (`EoP`) of the selected track;
- information on possible activity in the MUV3 detector associated with the selected track.

These reconstructed quantities form the basis for the event and hit-level selections and classifications described in the following sections.

3.4 Event Selection in RICHAnalysis

After the Ke3 pre-selection described in Section 3.3, a further event selection is applied within the RICHAnalysis framework.

While the `ke3` event pre-selection already provides a high-purity $K^+ \to \pi^0 e^+ \nu$ sample, additional quality requirements are introduced to ensure optimal RICH performance and stable hit classification.

3.4.1 Definition of a Good Track

Within RICHAnalysis, the reconstructed charged particle is required to be uniquely associated with a reconstructed RICH ring and to satisfy timing consistency conditions with both the RICH detector and the experiment trigger.

The following requirements are applied:

$$|t_{\text{ring}} - t_{\text{RICH}}| < 2 \text{ ns},$$

$$|t_{\text{track}} - t_{\text{trigger}}| < 20 \text{ ns}.$$

3.4.2 Particle Identification Cuts

To further purify the positron candidate sample, additional particle-identification (PID) requirements are applied to the reconstructed charged track.

- **Calorimeter probabilities:** The likelihood-based calorimetric discriminants are required to satisfy

$$\texttt{CalProbElectron} > 0.80, \qquad \texttt{CalProbPion} < 0.10,$$

  minimising hadronic contamination.

- **Muon veto:** Events with activity in MUV3 associated with the candidate track are rejected, suppressing residual muon background.

- E/p **requirement:** At the final stage, a moderately wide window

$$0.94 < E/p < 1.06$$

  is imposed.

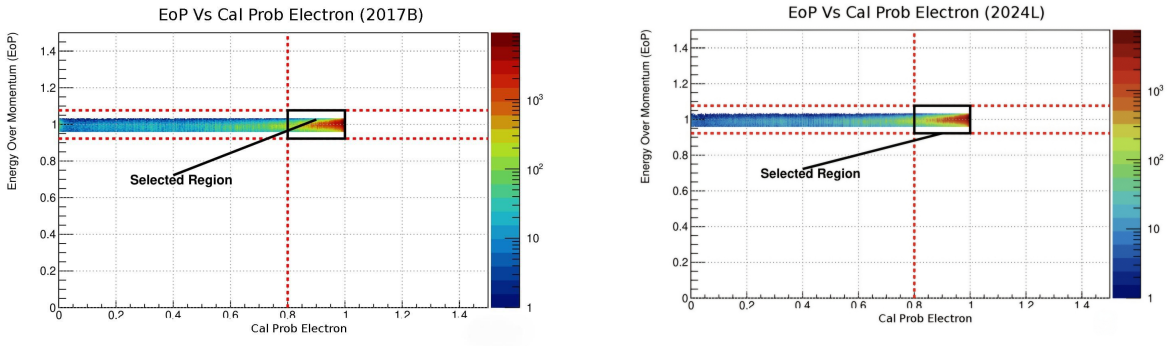

Figure 8: Correlation between energy-over-momentum ratio (E/p) and calorimetric electron-identification probability for 2017B (left) and 2024L (right). The selected region (whose boundaries are indicated by the dashed lines) corresponds to $0.94 < E/p < 1.06$ and CalProbElectron > 0.8 .

The distributions shown in Fig. 8 illustrate the correlation between the calorimetric electron probability and the energy-over-momentum ratio for the two data-taking periods. Events passing the selection criteria are used for the subsequent RICH analysis.

3.4.3 LKr Cluster Requirements

To ensure the presence of electromagnetic activity consistent with the $\pi^0 \to \gamma\gamma$ decay, additional requirements are imposed on clusters reconstructed in the LKr electromagnetic calorimeter.

At least two LKr clusters are required, each satisfying:

- reconstructed energy $E \geq 3$ GeV,
- cluster time within ± 40 ns of the trigger time,
- inter–cluster time difference smaller than 10 ns.

3.5 Overview of the Workflow

After the event selection described in Section 3.4, each accepted event is analysed using the reconstructed RICH information.

For every selected event, the RICH reconstruction provides:

- a list of photon hits on the PMT plane, each characterised by:
  - PMT coordinates (x_i, y_i) in the PMT plane,
  - calibrated detection time t_{hit},
  - PMT identifier and quality flags;
- a reconstructed Cherenkov ring associated with the selected track, defined by:
  - ring centre coordinates (x_c, y_c),
  - ring radius R,
  - t_{ring}: the reconstructed ring time,
- a global RICH reference time t_{RICH}.

The analysis proceeds through the following steps:

1. definition of timing observables derived from the reconstructed quantities;
2. hit selection based on temporal cuts;
3. classification of selected RICH hits as clean or spurious based on spatial criteria;

4. classification of events according to the multiplicity of spurious hits.

The geometrical and timing definitions used in this procedure are described in detail in the following sections.

3.6 Hit Classification

3.6.1 Timing Observables and Hit Selection

The RICH reconstruction provides timing information defined at both the hit and event level. These quantities are used to assess the temporal consistency of photon hits associated with a given event.

For each detected photon hit, the calibrated detection time t_{hit} is available. This quantity is defined individually for each hit recorded on the RICH photomultiplier plane.

At the event level, the reconstructed Cherenkov ring is characterised by a ring time t_{ring}, obtained from a track–seeded fit as a weighted average of the times of hits associated with the ring. In addition, the RICH timing system provides a global reference time t_{RICH} for the event, synchronised with the experiment trigger.

Temporal information provides a powerful criterion to reject temporally inconsistent hits originating from accidental activity, including dark counts and electronic noises. To be accepted, a hit must satisfy

$$|t_{\mathrm{hit}} - t_{\mathrm{ring}}| < 2 \text{ ns} \qquad \text{and} \qquad |t_{\mathrm{hit}} - t_{\mathrm{RICH}}| < 2 \text{ ns}. \tag{3.1}$$

Figures 9 and 10 show the distributions of the hit–event time differences $|t_{\mathrm{hit}} - t_{\mathrm{RICH}}|$ and $|t_{\mathrm{hit}} - t_{\mathrm{ring}}|$, computed for all the photon hits.

Figure 11 shows the distribution of $|t_{\mathrm{ring}} - t_{\mathrm{RICH}}|$ for the reconstructed rings.

3.6.2 Hit Radial Residual And Hit Classification

The key geometrical quantity for classifying hits is the radial residual, defined for each hit i as

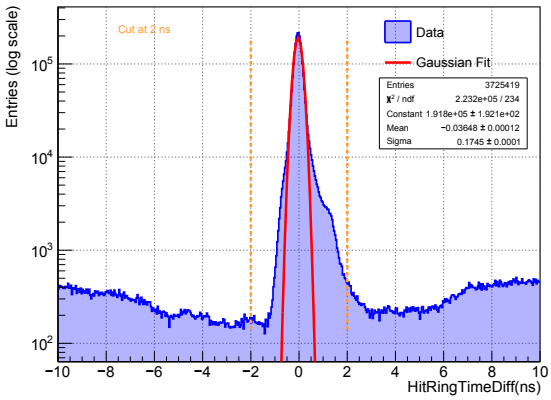

Figure 9: Distribution of $|t_{\text{hit}} - t_{\text{RICH}}|$ for RICH hits. The vertical dashed lines indicate the ± 2 ns timing selection applied in the analysis.

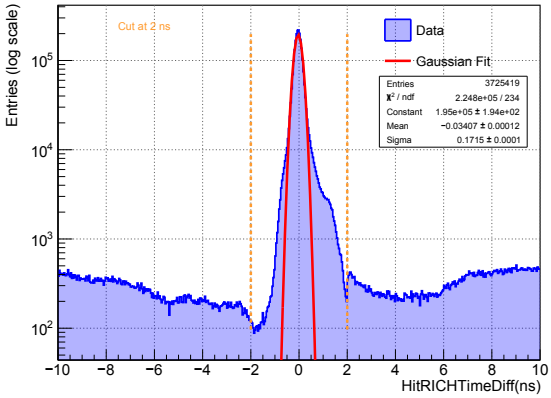

Figure 10: Distribution of $|t_{\text{hit}} - t_{\text{ring}}|$ for RICH hits. The vertical dashed lines indicate the ± 2 ns timing selection applied in the analysis.

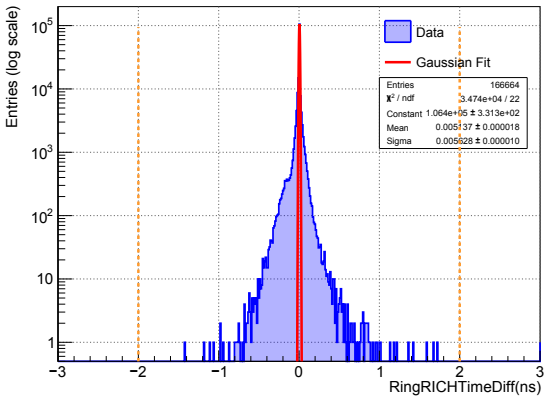

Figure 11: Distribution of $|t_{\text{ring}} - t_{\text{RICH}}|$ for reconstructed RICH rings.

$$\Delta r_i = \sqrt{(x_i - x_c)^2 + (y_i - y_c)^2} - R_{\text{fit}}, \tag{3.2}$$

where R_{fit} is the reconstructed ring radius obtained from the ring fit. Hits located exactly on the reconstructed ring satisfy $\Delta r_i = 0$.

In an ideal detector, the Δr distribution for genuine Cherenkov photons would be centred at zero, with a width determined by:

- the photomultiplier pitch (18 mm) and light-collection geometry;
- chromatic dispersion of the radiator gas ($n = n(\lambda)$ leading to $\theta_C = \theta_C(\lambda)$);
- multiple Coulomb scattering of the charged particle while traversing the radiator;
- residual mirror-alignment and focal-length uncertainties.

Figure 12 shows the distribution of the radial residual Δr defined in Eq. (3.2). The distribution exhibits a narrow peak around zero and extended tails at larger values.

Hits are classified using the condition

$$|\Delta r_i| \leq 15 \text{ mm} \tag{3.3}$$

Using the spatial criteria above, we define:

- **Clean hit:** a selected hit is labelled clean if it satisfies equation (3.3)
- **Spurious hit:** any selected hit that fails the condition in equation (3.3).

Once individual hits have been classified, the event as a whole can be characterised according to the amount of spurious hits it contains.

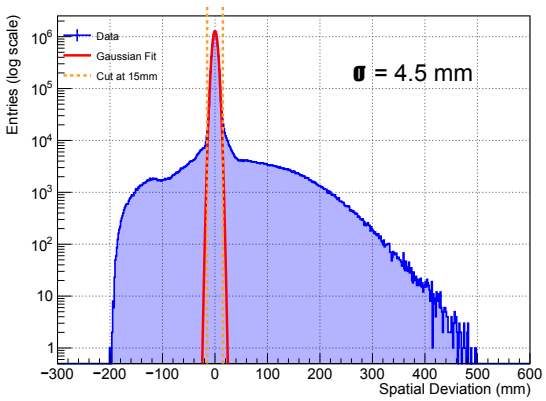

Figure 12: Distribution of the radial residual Δr for RICH hits. The vertical dashed lines indicate the boundary used to classify hits as clean or spurious.

3.7 Event Classification and Spurious Hit Multiplicity

Let N_{hit} be the total number of in-time hits in an event and N_{spurious} the corresponding number of spurious hits.

An event is classified as:

- **Clean event:** $N_{\text{spurious}} = 0$;
- **Spurious event:** $N_{\text{spurious}} \geq 1$.

To quantify the amount of spurious hits, spurious events are further subdivided according to the multiplicity N_{spurious}:

$$N_{\text{spurious}} = 1 \tag{3.4}$$

$$N_{\text{spurious}} = 2 \tag{3.5}$$

$$N_{\text{spurious}} \geq 3 \tag{3.6}$$

These definitions form the basis for the comparative analysis presented in Chapter 4.

4. Results and Comparative Analysis

This chapter presents the results of the spurious–hit analysis. All reconstruction procedures, selection criteria, and classification definitions are fixed *a priori* and are not re–optimised here. The emphasis is instead placed on a comparative study of the 2017B and 2024L data sets, with the goal of identifying changes in spurious–hit behaviour and understanding their origin.

In the following discussion, the term *mirror* refers to an individual mirror segment, while the term *mirror plane* denotes the complete set of mirrors forming the reflective surface of the RICH detector.

4.1 Spurious-Hit Multiplicity and Event Statistics

4.1.1 Spurious-Hit Multiplicity Distributions

Figure 13 shows the distribution of the number of spurious hits per event for all selected events in the 2017B and 2024L run periods.

The distributions are strongly peaked at low multiplicities, with a dominant population of clean events ($N_{\text{spurious}} = 0$). Events containing one or two spurious hits form a small but non-negligible fraction, while higher multiplicities are increasingly suppressed.

Despite differences in overall spurious activity between 2017B and 2024L, the qualitative shape of the multiplicity distributions remains similar.

4.1.2 Event and Hit Yields

The total numbers of reconstructed events and associated RICH hits after all selection criteria are summarised in Table 1.

A key observation is that, although spurious events are defined by the presence of at least one spurious hit, the majority of hits within these events are still clean. In both run periods,

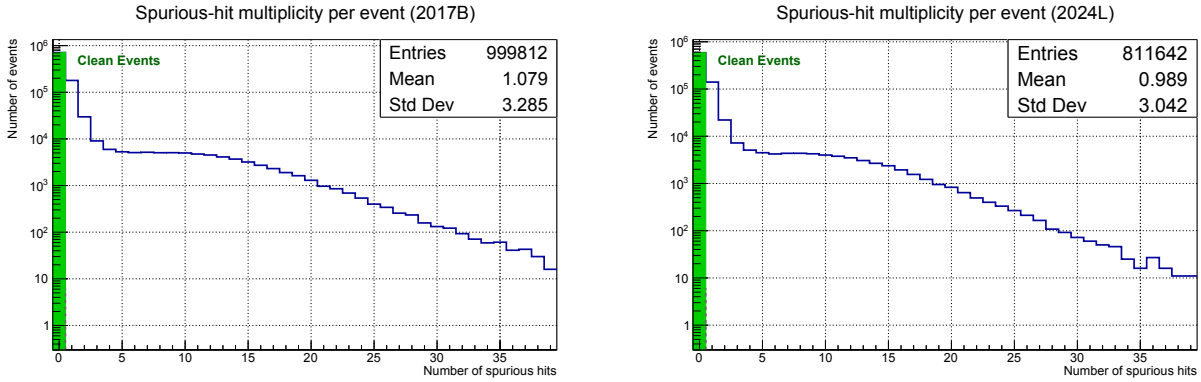

Figure 13: Spurious hit multiplicity per event for 2017B (left) and 2024L (right) run periods.

Table 1: Event and hit statistics after all selection criteria.

	Events (2017B)	**Hits (2017B)**	**Events (2024L)**	**Hits (2024L)**
Total (after all cuts)				
Total	999,812	13,769,303	811,642	10,379,724
Clean events				
Clean events	709,862		586,456	
Clean hits		8,950,146		6,873,968
Spurious events				
Spurious events	289,950		225,186	
Clean hits		3,737,368		2,701,569
Spurious hits		1,081,789		804,187

clean hits in spurious events outnumber spurious hits by more than a factor of three.

This indicates that spurious hits constitute a small fraction of the total hit population and are not the dominant contribution to the event sample as a whole.

This behaviour is further illustrated in Fig. 14, which shows the distributions of the number of clean RICH hits per event for clean and spurious events in the 2017B and 2024L run periods. For both periods, the clean-hits distribution in spurious events closely resemble those observed in clean events, with only minor differences in shape and mean value. This confirms that the presence of spurious hits does not significantly distort the overall clean-hit multiplicity associated with the reconstructed Cherenkov ring.

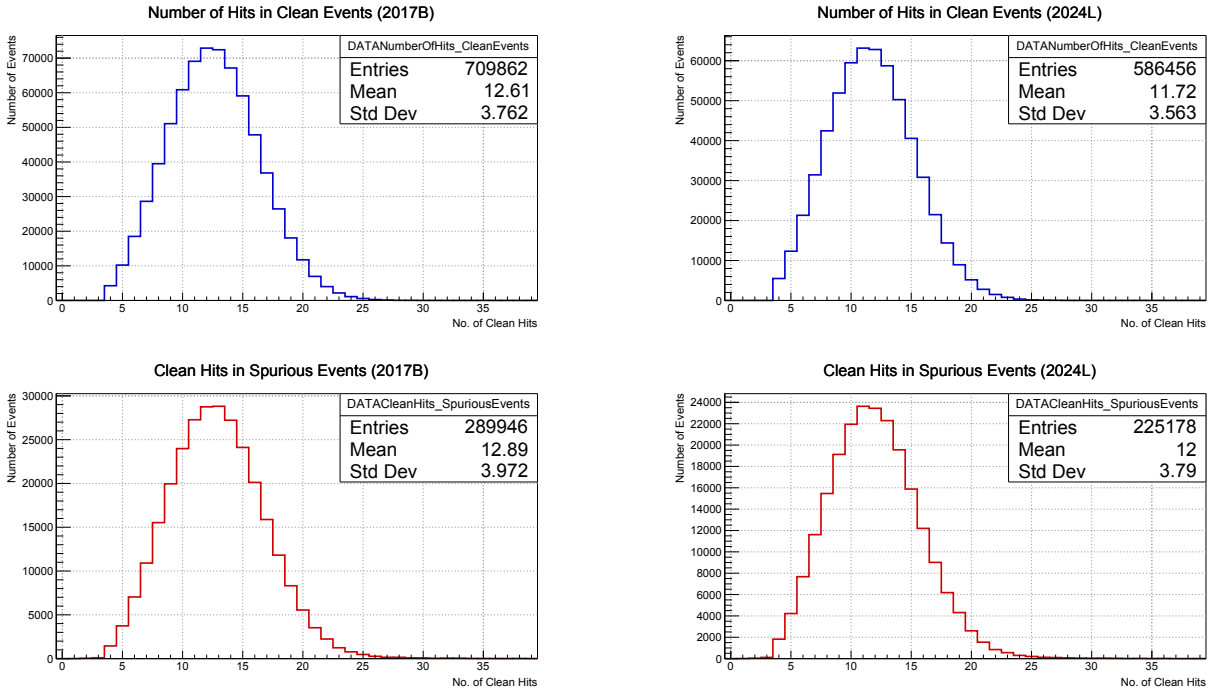

Figure 14: Distributions of the number of clean RICH hits per event for clean events (top row) and spurious events (bottom row), shown for the 2017B(left) and 2024L(right) run periods.

4.1.3 Spurious-Event and spurious-hit multiplicities

Table 2 summarises the number of spurious events and the average number of spurious hits per event for different spurious hit multiplicity categories. For events with $N_{\text{spurious}} > 2$, the average number of spurious hits per event is substantially larger than in the $N_{\text{spurious}} = 1$ and $N_{\text{spurious}} = 2$ categories.

Table 2: Spurious-event categories and average spurious-hit multiplicities.

	2017B		2024L	
Category	**Events**	$\langle N_{\text{spurious}} \rangle$	**Events**	$\langle N_{\text{spurious}} \rangle$
$N_{\text{spurious}} = 1$	179,246	1.0	140,206	1.0
$N_{\text{spurious}} = 2$	29,757	2.0	22,089	2.0
$N_{\text{spurious}} > 2$	80,947	10.4	62,891	9.8

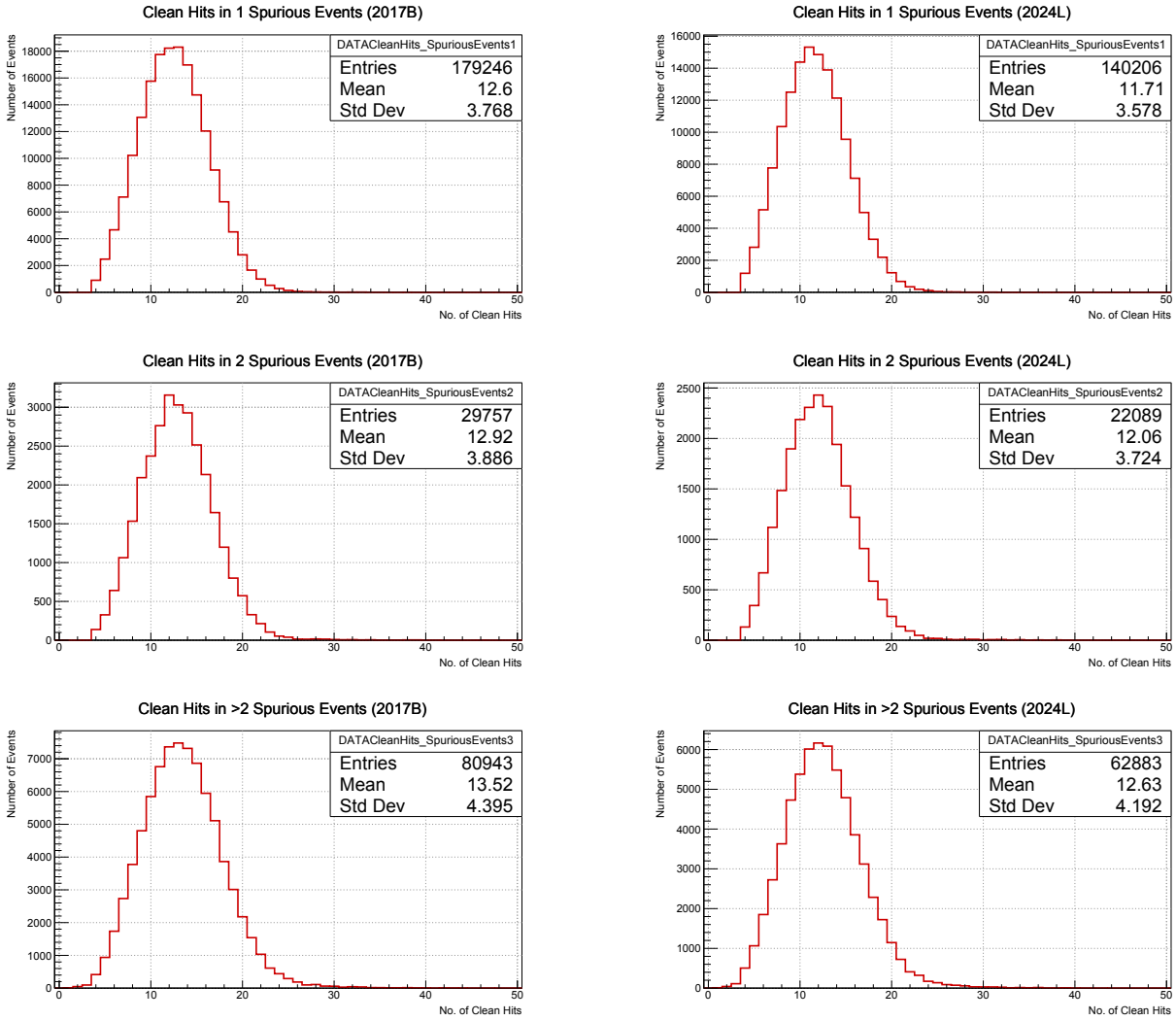

Figure 15: Distributions of the number of clean RICH hits per event for different spurious-hit multiplicity categories. The three rows correspond to events with $N_{\text{spurious}} = 1$, $= 2$, and > 2, while the two columns show the 2017B and 2024L run periods.

4.1.4 Average Number of Clean Hits per Event

Figure 15 displays the distributions of the clean-hit multiplicity for the different spurious-hit categories in the 2017B and 2024L run periods.

Table 3: Average number of clean hits per event.

Event category	**2017B**	**2024L**
Clean events	12.61	11.72
Spurious events, $N_{\text{spurious}} = 1$	12.60	11.71
Spurious events, $N_{\text{spurious}} = 2$	12.92	12.06
Spurious events, $N_{\text{spurious}} > 2$	13.52	12.63

The average number of clean hits per event for the different event categories is summarised in Table 3. For both run periods, the clean-hit multiplicity is nearly identical for clean events and for events with $N_{\text{spurious}} = 1$. For larger spurious-hit multiplicities, the average number of clean hits per event increases moderately.

4.1.5 Hit Position on the PMT plane

To investigate the spatial characteristics of spurious activity in the RICH detector, the positions of spurious hits on the merged PMT plane are studied for events with different spurious-hit multiplicities.

Figure 16 shows two-dimensional maps of spurious-hit positions for events containing one, two, and more than two spurious hits, displayed separately for the 2017B and 2024L run periods.

For events with one or two spurious hits, the spurious-hit position distributions exhibit a broadly uniform occupancy across the merged PMT plane, without pronounced spatial asymmetries. In contrast, events with $N_{\text{spurious}} > 2$ display a markedly different pattern: a concentration of spurious hits appears on one side of the detector, accompanied by a ring-like structure that is absent in the lower-multiplicity categories.

The presence of this structured spatial pattern indicates that high-multiplicity spurious events are not purely the result of isolated random noise. A more detailed investigation of this behaviour is presented in the following section, where the spurious-hit distributions are analysed separately in the Jura and Salève regions of the detector.

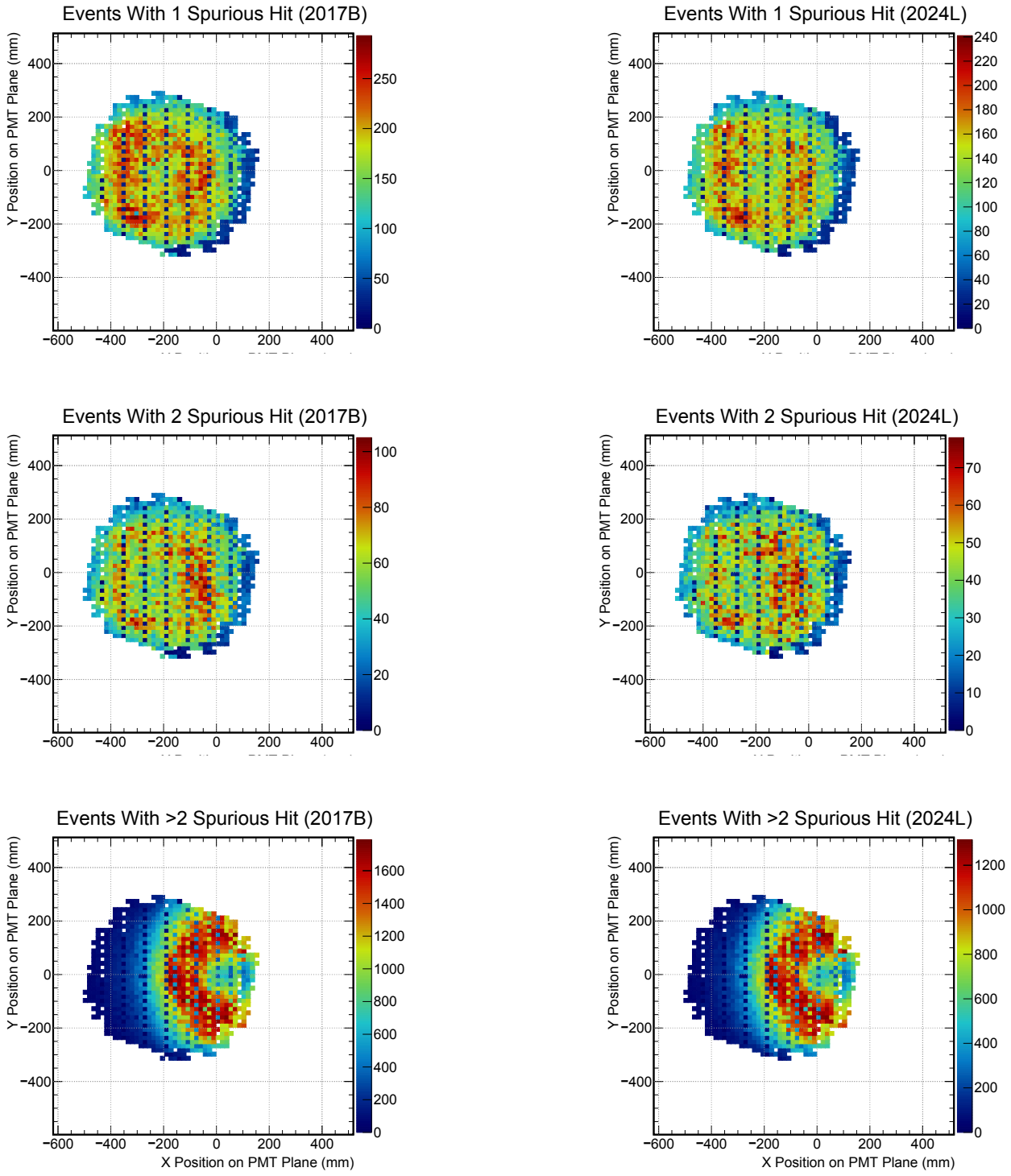

Figure 16: Hit-position distributions on the merged PMT plane for events with $N_{\text{spurious}} = 1$, $N_{\text{spurious}} = 2$, and $N_{\text{spurious}} > 2$. The two columns correspond to the 2017B (left) and 2024L (right) run periods.

4.1.6 Spurious Hit Positions on Jura and Salève region

To further investigate the spatial characteristics of spurious activity, the spurious-hit position distributions on the PMT regions are studied separately for the Jura and Salève regions of the detector (see Sec. 2.4). Figure 17 presents the corresponding two-dimensional maps for the 2024L run periods,, shown for events with $N_{\text{spurious}} = 1$, $N_{\text{spurious}} = 2$, and $N_{\text{spurious}} > 2$.

For events with $N_{\text{spurious}} = 1$ and $N_{\text{spurious}} = 2$, the spurious-hit occupancy on the Salève side is visibly higher than on the Jura side. In these categories, the spatial distributions appear relatively diffuse and do not exhibit pronounced localised structures.

In contrast, events with $N_{\text{spurious}} > 2$ show a qualitatively different topology. On the Jura side, a strong concentration of spurious hits is observed, forming a ring-like structure that is not present in the lower-multiplicity categories.

4.2 Track Impact Position on the RICH Mirror Plane

Figure 18 shows the two-dimensional distributions of the extrapolated track impact position on the RICH mirror plane for clean events and for events containing spurious hits, displayed separately for the 2017B and 2024L run periods.

For clean events, the distributions exhibit an approximately up–down symmetric pattern with respect to the horizontal plane containing the beam axis. The observed pattern reflects the geometrical acceptance of the RICH mirror system for the selected event sample.

In contrast, events containing spurious hits exhibit a different distribution of track impact positions. In particular, a larger population of events appears in the lower region of the mirror plane, leading to a visible asymmetry between the upper and lower regions. This feature motivates a more detailed investigation of the spatial properties of events containing spurious hits, which is presented in the following section.

4.2.1 Distribution of Cherenkov photons around the track position

For a charged particle traversing the RICH radiator, Cherenkov photons are emitted at an approximately constant rate along the particle trajectory. Photons produced within a given segment of the track propagate to the mirror system, where their impact points form a ring-shaped region centred at the extrapolated track impact position P on the RICH mirror

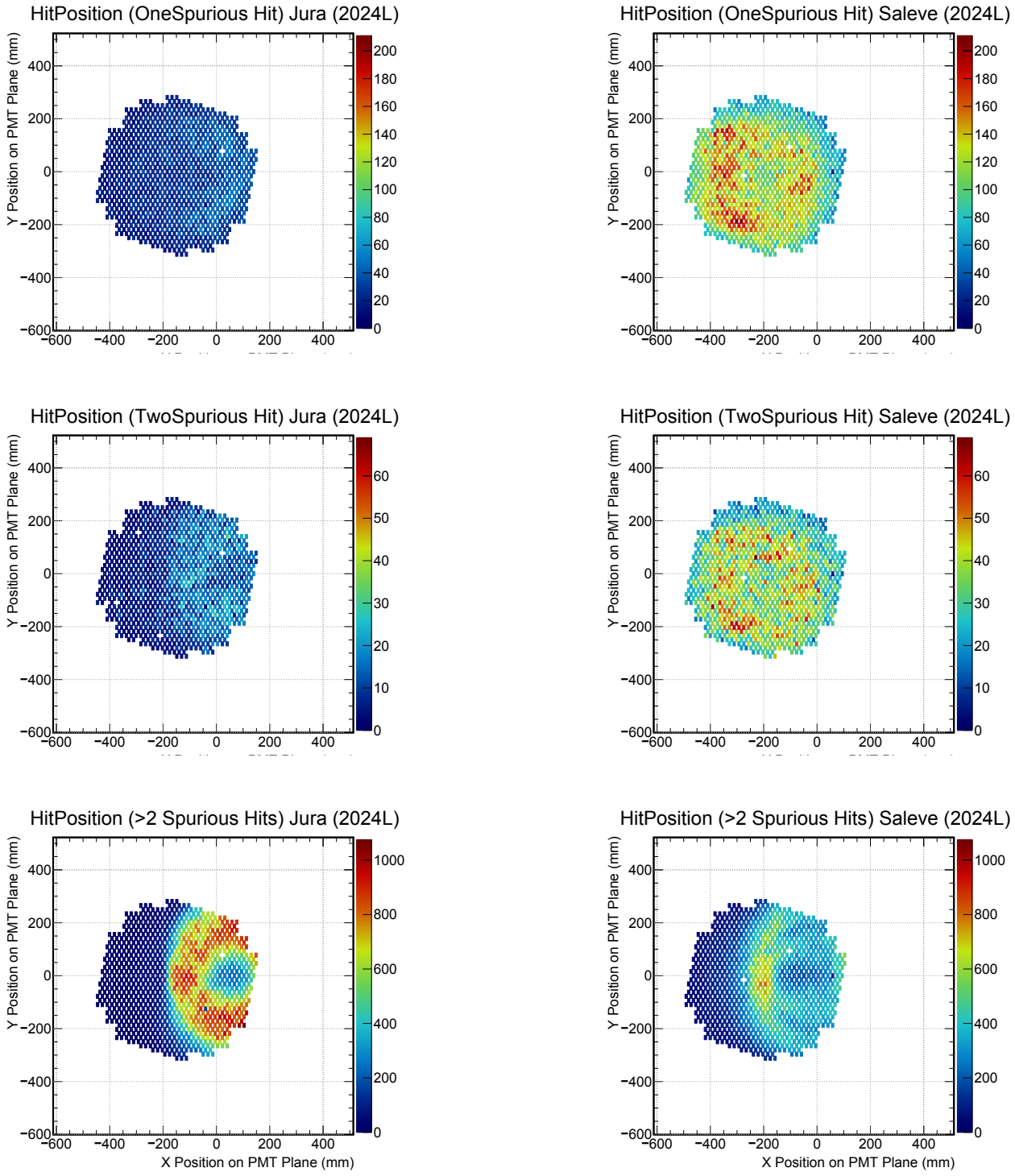

Figure 17: Spatial distributions of spurious hits on the Jura and Salève PMT regions for events with $N_{\text{spurious}} = 1$, $N_{\text{spurious}} = 2$, and $N_{\text{spurious}} > 2$ for 2024L run period. The two columns correspond to the Jura (left) and Salève (right) regions of the detector.

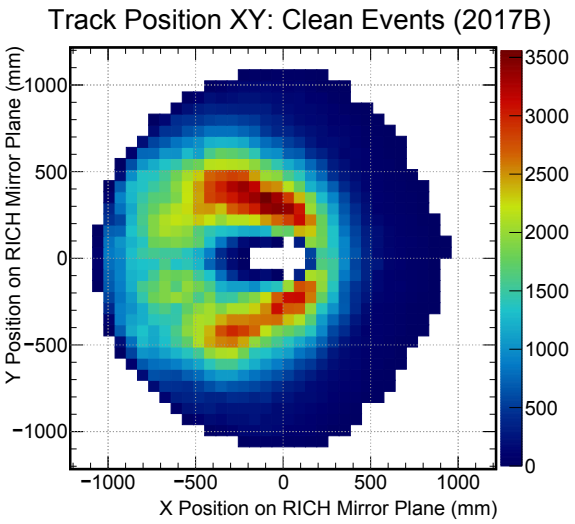

((a)) Clean events (2017B)

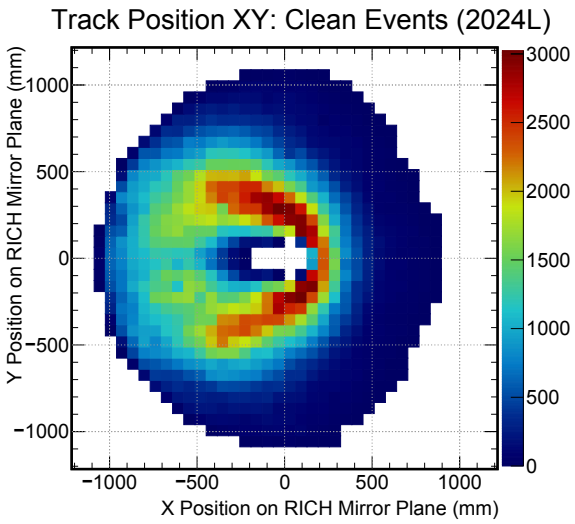

((b)) Clean events (2024L)

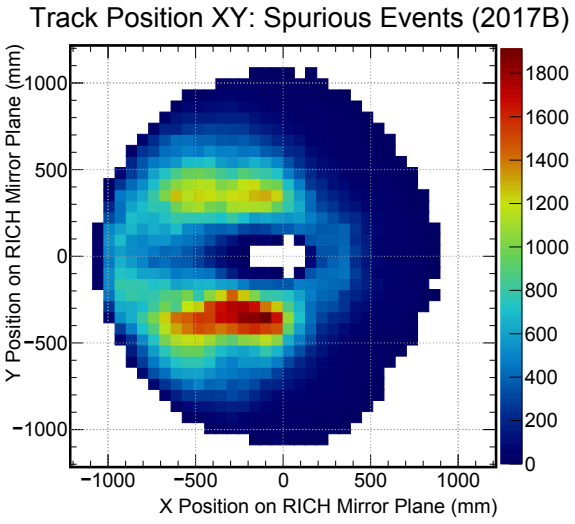

((c)) Spurious events (2017B)

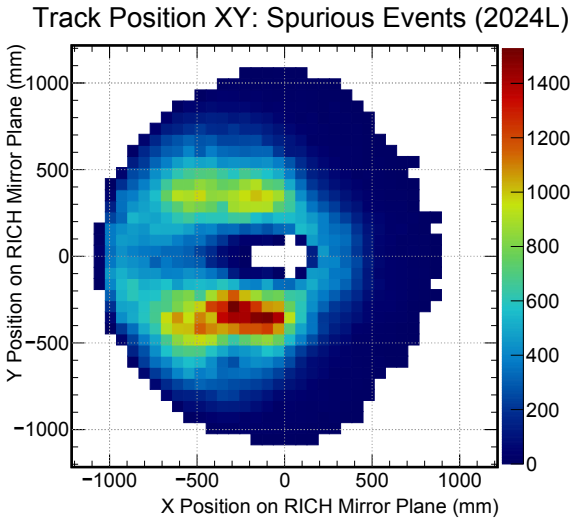

((d)) Spurious events (2024L)

Figure 18: Distribution of the extrapolated track positions on the RICH mirror plane. The four panels correspond to clean events (top row) and spurious events (bottom row) for the 2017B (left column) and 2024L(right column) run periods.

plane.

Equal path-length segments along the trajectory correspond to rings of equal radial width on the mirror plane. Consequently, the radial photon yield satisfies

$$\frac{dN_\gamma}{dr} \simeq \text{const.} \tag{4.1}$$

Since the corresponding area element is $dA = 2\pi r\, dr$, the photon surface density on the mirror plane scales as $\rho(r) \propto 1/r$. Consequently, spatial observables expressed as functions of the extrapolated track impact position (X_p, Y_p) receive a larger contribution from photons reflected in the vicinity of the track impact point.

By selecting events according to the extrapolated track impact position on the mirror plane, the analysis probes localized regions of the RICH mirror surface with centimeter-scale sensitivity. This makes it possible to study region-dependent effects such as variations in mirror reflectivity, borders between mirror segments, localized surface defects, or small alignment distortions. All spatial distributions presented in this section are expressed as functions of the extrapolated track position on the RICH mirror plane.

4.2.2 Average Number of Clean Hits as a Function of Track Position

The average number of clean RICH hits is studied as a function of the extrapolated track impact position on the RICH mirror plane in order to investigate possible position–dependent variations in the detector response. Figure 19 shows two-dimensional maps of this quantity as a function of (X_p, Y_p), independently of the local track density on the mirror plane.

For each bin in the (X_p, Y_p) plane, the average number of clean hits per event is computed using all events whose extrapolated track intersects the corresponding region of the mirror plane. These maps therefore provide a local measurement of the average clean-hit yield as a function of the track impact position on the RICH mirror plane.

Position-dependent variations are observed across the mirror plane. Regions with larger average values correspond to positions where a larger number of clean hits are detected per event, while regions with smaller values correspond to positions where fewer clean hits are detected.

A comparison between the two run periods shows that the spatial pattern of the average clean-hit yield is similar in both cases. However, the overall average number of clean hits per event is larger in the 2017B run period than in the 2024L run period, as already observed in Table 3.

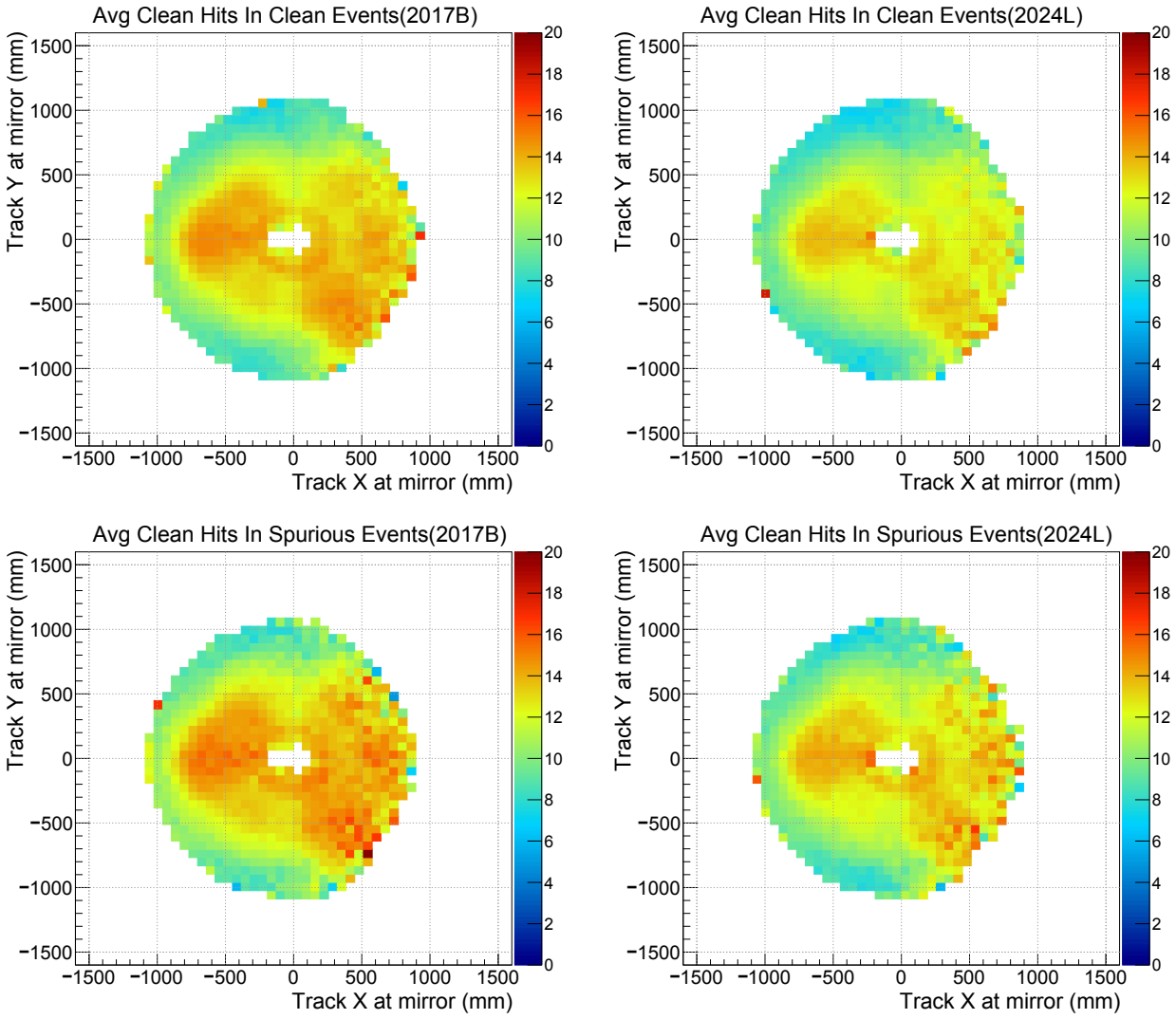

Figure 19: Distribution of the average number of clean RICH hits per event as a function of the extrapolated track impact position (X_p, Y_p) on the RICH mirror plane. The left column corresponds to the 2017B run period and the right column to the 2024L run period. The upper row shows clean events, while the lower row shows spurious events.

4.2.3 Spurious-Event Fraction and Mirror Segmentation Layout

Since the distribution of extrapolated track positions on the mirror plane is not uniform, the spatial behaviour is studied by considering the fraction of spurious events, $x_{\text{spurious}} = N(\text{spurious events})/N(\text{all events})$, as a function of the extrapolated track impact position

(X_p, Y_p). This quantity provides an estimate of the probability for an event to contain spurious hits, independently of the local track density on the mirror plane and therefore provides an estimate of the probability for an event to contain spurious hits as a function of (X_p, Y_p).Figure 20 shows the corresponding maps of the spurious-event fraction x_{spurious} for the 2017B and 2024L run periods together with the RICH mirror segmentation layout.

Regions with larger values of the spurious–event fraction are observed near several mirror boundaries.In particular, pronounced structures appear near some mirror boundaries of mirrors. The structure particularly pronounced along all edges of mirror 14 and along the left side of mirror 5, while weaker structures are observed near the boundaries of mirrors 3 and 20. The spatial correspondence between these features and the mirror segmentation indicates that events with tracks intersecting these mirror-boundary regions have a higher probability of containing spurious hits.

The presence of similar structures in both run periods indicates that these features are stable in time and are related to the behaviour of the mirror system.

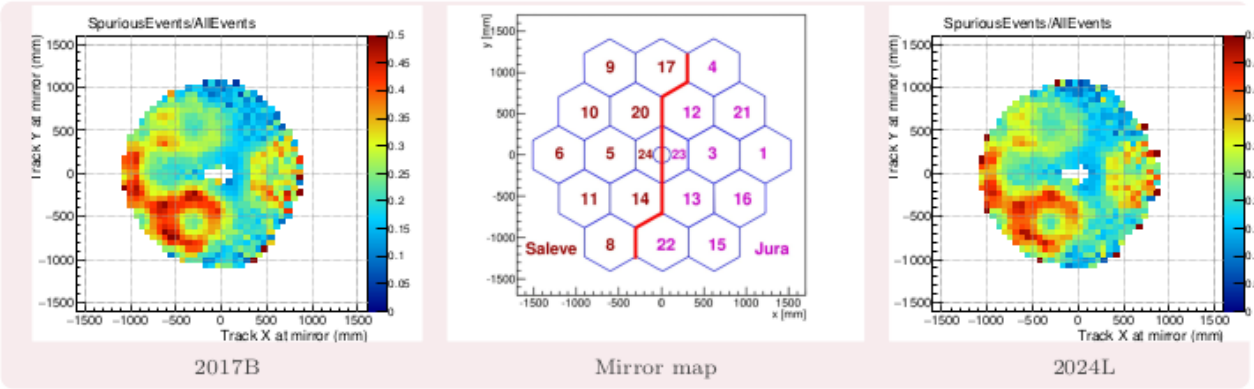

Figure 20: Fraction of spurious events, x_{spurious}, as a function of track impact position (X_p, Y_p) on the mirror plane for 2017B(left) and 2024L(right). The central figure shows the mirror segmentation map.

To further characterise the nature of spurious-hit production, events are subdivided according to the number of spurious hits they contain. The spatial distributions for events with $x_{\text{spurious}} = 1$, $x_{\text{spurious}} = 2$, and $x_{\text{spurious}} > 2$ are shown in Figure 21 for both run periods. The fraction of events containing one or two spurious hits is significantly higher than its average values along specific mirror boundaries, consistent with localised imperfections of the reflecting surface. In contrast, events with more than two spurious hits display a broader and more

diffuse spatial distribution across the mirror surface, indicating a qualitatively different origin for high-multiplicity spurious activity.

4.3 Straw–RICH Consistency

The STRAW spectrometer reconstructs the downstream track momentum vector after the magnet, $\vec{p} = (p_x, p_y, p_z)$. The STRAW track slopes are defined as

$$s_x^{\mathrm{STRAW}} = \frac{p_x}{p_z}, \qquad s_y^{\mathrm{STRAW}} = \frac{p_y}{p_z}, \tag{4.2}$$

which encode the track direction with respect to the beam axis.

On the RICH side, under the small-angle approximation, the track direction can be inferred from the reconstructed ring centre coordinates. The corresponding slopes are defined as

$$s_x^{\mathrm{RICH}} = \frac{x_c}{f}, \qquad s_y^{\mathrm{RICH}} = \frac{y_c}{f}, \tag{4.3}$$

where $f = 17$ m is the focal length of the RICH mirror system.

The slope differences are then defined as

$$\Delta s_x = s_x^{\mathrm{RICH}} - s_x^{\mathrm{STRAW}}, \qquad \Delta s_y = s_y^{\mathrm{RICH}} - s_y^{\mathrm{STRAW}}. \tag{4.4}$$

Figure 22 shows the distributions of the track slopes reconstructed independently by the STRAW spectrometer and by the RICH detector.

Figure 23 presents the distributions of the slope differences Δs_x and Δs_y, as well as their correlations with the STRAW-measured slopes.

The agreement between the two measurements demonstrates the overall geometrical con-

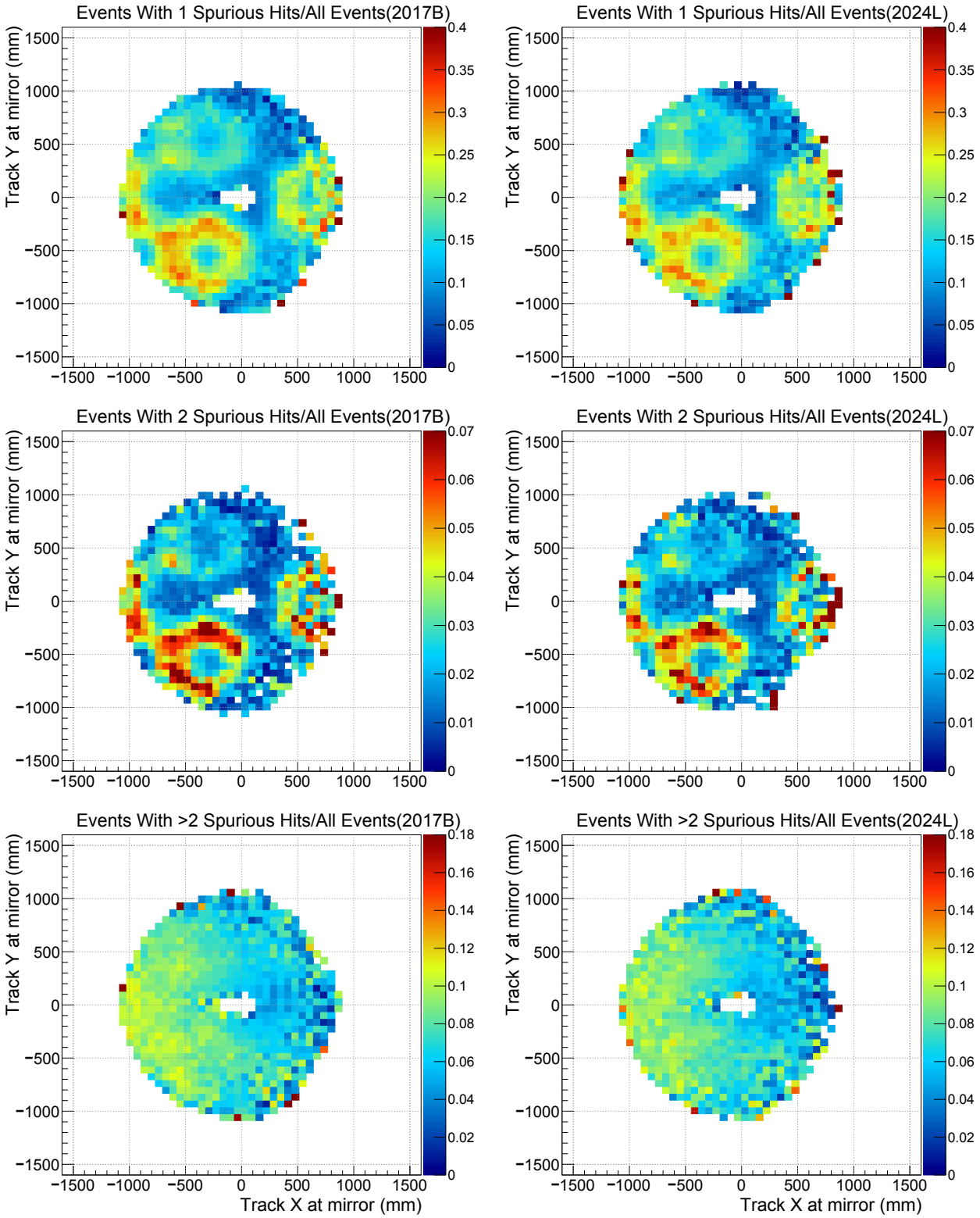

Figure 21: Fraction of events with $x_{\text{spurious}} = 1$, $x_{\text{spurious}} = 2$, and $x_{\text{spurious}} > 2$, expressed as fractions of the total number of events in each bin of the extrapolated track impact position (X_p, Y_p) on the RICH mirror plane. The left column corresponds to the 2017B run period and the right column to the 2024L run period.

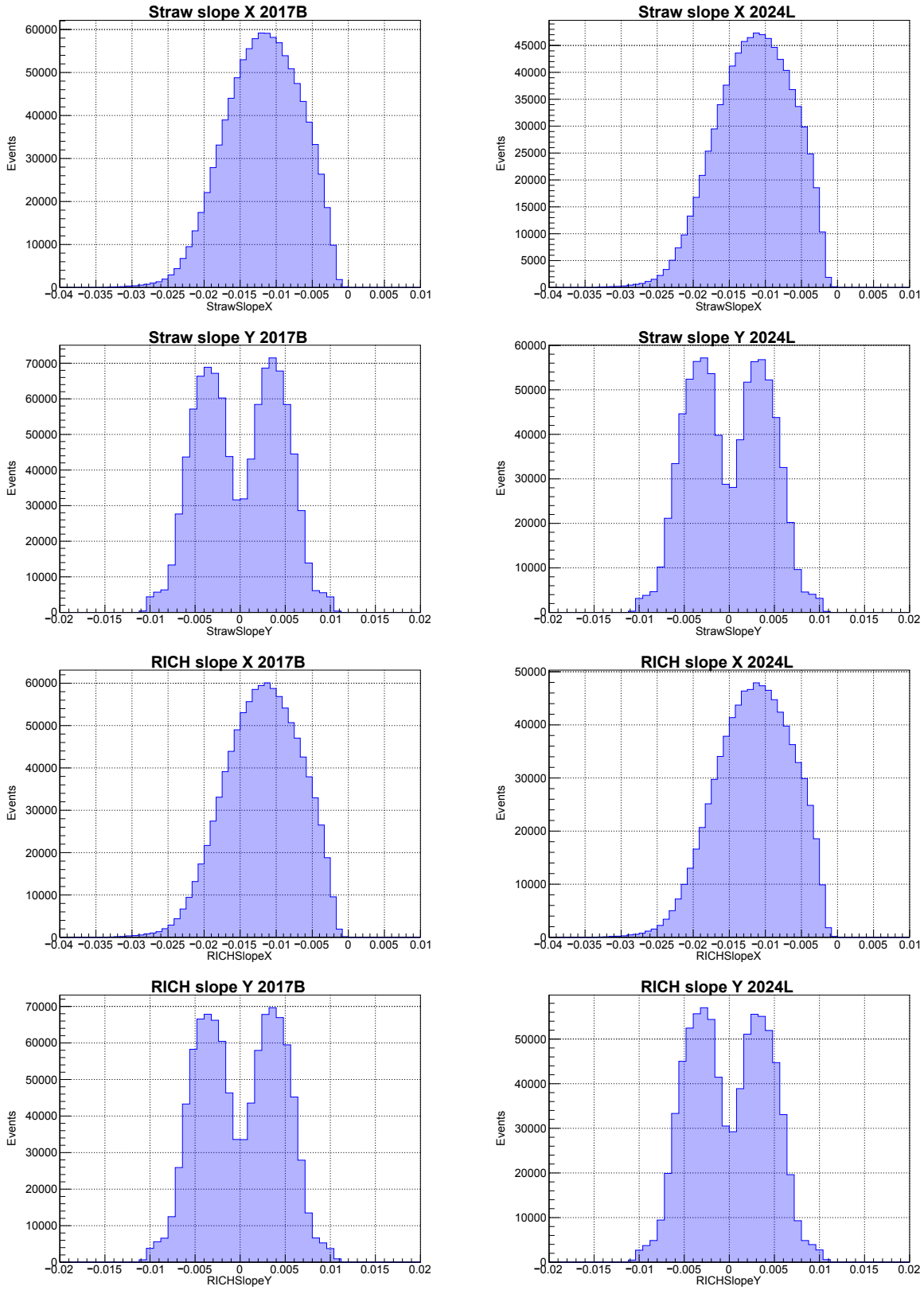

Figure 22: Track-slope distributions in the horizontal (s_x) and vertical (s_y) projections for slopes reconstructed using the STRAW spectrometer and the RICH ring reconstruction. The left column corresponds to the 2017B run periods and the right column to the 2024L run periods.

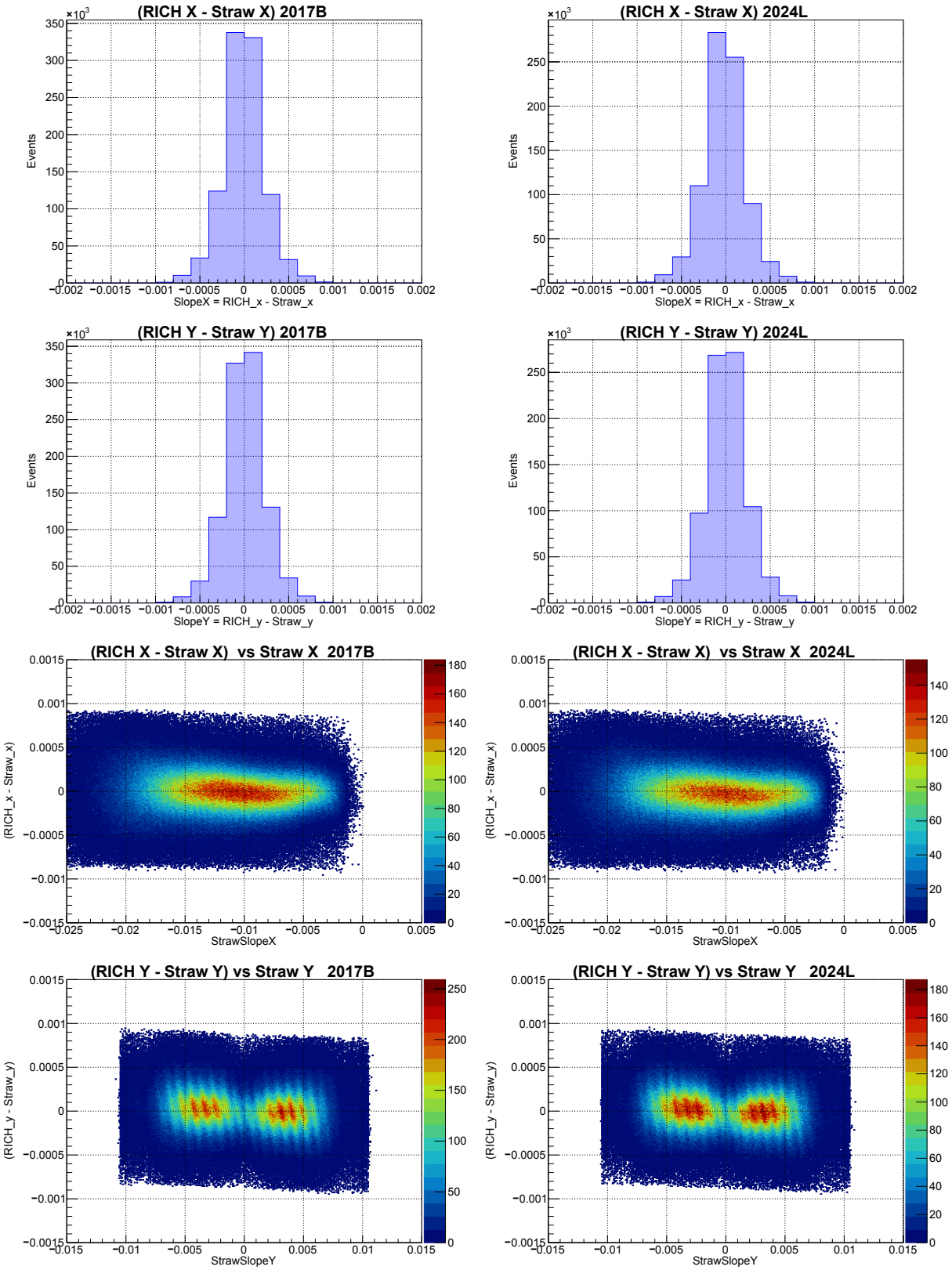

Figure 23: Slope differences between the RICH- and STRAW-derived track slopes. The first two rows show the one-dimensional distributions of Δs_x and Δs_y. The last two rows show the correlations Δs_x vs s_x^{STRAW} and Δs_y vs s_y^{STRAW}. The left column corresponds to the 2017B run period and the right column to the 2024L run period.

sistency between the STRAW and RICH reconstruction and indicates that detector misalignment or reconstruction biases do not significantly affect the determination of the track direction.

5. Conclusions

5.1 Summary of Findings

The study of spurious-hit behaviour in the RICH detector leads to the following observations.

Event classification. Events were grouped according to the number of spurious hits, $k = \{0, 1, 2, > 2\}$, corresponding respectively to clean events ($k = 0$), events with one or two spurious hits ($k = 1, 2$), and high-multiplicity spurious events ($k > 2$). This classification provides a structured framework for comparing events with different levels of spurious hits content.

Multiplicity behaviour. The high-multiplicity category ($k > 2$) represents a small fraction of the total event sample, amounting to about 8% in both the 2017B and 2024L run periods. The similarity of this fraction in the two periods indicates that the mechanisms responsible for high spurious multiplicities are not strongly affected by the different running conditions. In particular, although the beam intensity differed between the two periods, this comparison suggests that the dominant sources of high-multiplicity spurious hits are not directly driven by the beam rate.

Clean-hit content. The average number of clean hits per event shows a mild dependence on the spurious-hit multiplicity:

- For $k = 0$ and $k = 1$, the average clean-hit yield is consistent within statistical uncertainties.
- For $k = 2$, the average clean-hit yield increases by approximately $+0.3$ hits per event relative to $k = 0$.
- For $k > 2$, a larger increase of about $+0.9$ clean hits per event is observed.

This behaviour is compatible with the presence of additional photon activity in high-multiplicity events. In such cases, the majority of extra photons are classified as spurious, while a small fraction may be reconstructed close to the nominal ring radius and therefore be classified as

clean by chance.

When comparing the two run periods, the average clean-hit yield is lower in 2024L by approximately 0.9 hits per event. This difference is unlikely to be directly related to the beam intensity and may instead reflect long-term variations in the average number of Cherenkov photons detected per positron ring.

Spurious-hit content. For events with $k > 2$, the average number of spurious hits per event decreases slightly from 10.4 in 2017B to 9.8 in 2024L. The most significant feature of this category is not the small variation between run periods but the fact that the average multiplicity is significantly large, this might indicate the presence of additional charged tracks produced in a multibody kaon decay.

Track-position dependence. The spatial distribution of spurious-event fractions was studied as a function of the extrapolated track impact position (X_p, Y_p) on the RICH mirror plane. Events containing one or two spurious hits exhibit enhanced probability in regions located near specific mirror boundaries. This observation suggests that a substantial fraction of low-multiplicity spurious hits is associated with local instrumental effects related to mirror segmentation.

5.2 Detector Alignment Validation

The relative alignment between the RICH detector and the STRAW spectrometer was assessed by comparing track slopes reconstructed independently by the two subsystems.

The distributions of the slope differences in both horizontal and vertical projections are centred around zero. This behaviour indicates consistency between the geometrical reconstruction provided by the two detectors and confirms that detector misalignment is not a dominant source of spurious-hit patterns.

5.3 Outlook

The analysis shows that a significant fraction of spurious hits is associated with well-defined regions near some mirror boundaries, pronounced structures appear near the boundaries of the mirrors 5, 6, and 14. These regions appear consistently in both the 2017B and 2024L run periods, suggesting stable detector conditions over time.

A. RICH Analysis Implementation

This appendix documents the software implementation of the RICH hit reconstruction, classification, and event–level analysis used throughout this thesis. The code is developed within the NA62 RICHAnalysis framework and is included here for completeness and reproducibility.

All physics definitions, selection criteria, and observables are introduced and motivated in Chapter 3, while the corresponding results and comparisons are presented in Chapter 4.

A.1 Environment and Execution

The analysis is executed within the NA62 software environment using the RICHAnalysis framework, which provides high–level access to reconstructed tracks, RICH rings, individual photon hits, and timing references.

The code is compiled locally, with runtime linking handled by configuring the shared–library path:

```
export LD_LIBRARY_PATH=/home/ayush/RICHAnalysis/lib_NA62Analysis
./RICHAnalysis -c config/ConfFile_richanalysis.txt \
              -o RICHAnalysis_2024.root
```

The configuration file specifies the data–taking period (2017B or 2024L), the enabled detector subsystems, and the list of histograms and TTrees written to the output ROOT file.

A.2 Event Processing Overview

The core of the analysis is implemented in the `RICHAnalysis::EventAnalysis()` method. Each event is processed according to the following logical sequence:

1. Retrieval of reconstructed particles and RICH hits.
2. Event preselection and basic quality requirements.

3. Positron identification using calorimetric and muon–veto information.
4. RICH ring validation using timing criteria.
5. Hit classification into clean or spurious categories.
6. Event classification based on spurious–hit multiplicity.
7. Filling of hit–level and event–level observables.

Only events satisfying all timing, particle–identification, and acceptance criteria contribute to the final analysis samples.

A.3 Event Initialization and Object Retrieval

At the beginning of each event, all per–event variables are reset and the reconstructed objects are retrieved from the NA62 event container:

```
ResetEvent();
fnEventsTot++;

fKPiPi0AEvent = GetKPiPi0AEvent();
fKaons = fKPiPi0AEvent->GetKPiPi0AUpstreamParticles();
fPions = fKPiPi0AEvent->GetKPiPi0ADownstreamChargedParticles();
fClusters = fKPiPi0AEvent->GetKPiPi0ADownstreamNeutralParticles();
fRICHHits = fKPiPi0AEvent->GetKPiPi0ARICHHits();
```

Events without at least one reconstructed charged track or without RICH hits are rejected at this stage.

A.4 Timing and Ring Validation

The event timing information is obtained from detector timing measurements associated with the reconstructed charged track. In particular, the RICH timing reference (`TRICH`) is used to define the event time. Consistency between the reconstructed RICH ring time and the global RICH timing reference (`TRICH`) is required:

```
double RingTime = Pion.GetRICHSingleRingTrkSeededTime();
double TRICH = Pion.GetTRICH();
```

```
bool hasRing = (RingTime > -100 && TRICH > -100);
if (!hasRing) return false;

bool isConsistentRingTime = (abs(RingTime - TRICH) < 2);
if (!isConsistentRingTime) return false;
```

This selection ensures that only rings temporally associated with the event are used in the analysis.

A.5 Positron Identification

Positrons are selected using calorimetric probabilities, the muon veto, and the energy–over–momentum ratio:

```
if (CalProbElectron <= 0.8) return false;
if (CalProbPion >= 0.1) return false;
if (MUV3Association) return false;
if (EoP < 0.94 || EoP > 1.06) return false;
```

These criteria define a high–purity positron sample and are fixed *a priori*, as described in Chapter 3.

A.6 Hit Classification

Each RICH hit is classified according to its spatial compatibility with the reconstructed ring and its timing consistency:

```
double distance = sqrt(pow(hitX - centerX, 2)
                     + pow(hitY - centerY, 2));
double deltaR = distance - RingRadius;

bool isValidHitTime =
    abs(hitTime - RingTime) < 2 &&
    abs(hitTime - TRICH) < 2;
```

```
bool isSpuriousHit = (abs(deltaR) > 15) && isValidHitTime;
bool isCleanHit = (abs(deltaR) <= 15) && isValidHitTime;
```

Hits failing the timing requirement are discarded. This definition exactly matches the one introduced in Section 3.8.

A.7 Event Classification

Event classification is performed after the hit classification loop, during which the number of spurious hits in the event is counted.

An event is defined as *spurious* if at least one hit satisfies the spurious–hit condition:

$$N_{\text{spurious}} \geq 1.$$

In the implementation, this condition is evaluated by accumulating the number of spurious hits in a dedicated counter:

```
bool hasSpuriousHits = false;
int spuriousHitCount = 0;

if (isSpuriousHit) {
    hasSpuriousHits = true;
    spuriousHitCount++;
}

bool isSpuriousEvent = hasSpuriousHits;
```

Spurious events are further subdivided according to the multiplicity of spurious hits ($N_{\text{spurious}} = 1, 2, \geq 3$), enabling the multiplicity–dependent studies presented in Chapter 4.

A.8 Jura–Salève Hit Separation

Hits are assigned to the Jura or Salève side of the detector based on their horizontal position:

```
bool isSaleve = IsSaleve(hitX);
bool isJura = !isSaleve;

if (isJura)
  fHisto->FillHisto(channel+"HitPosition_Jura", hitX, hitY);
else
  fHisto->FillHisto(channel+"HitPosition_Saleve", hitX, hitY);
```

This separation allows spatial asymmetries in spurious–hit activity to be studied independently in the Jura and Salève regions of the RICH detector.

A.9 RICH–Straw Slope Consistency

To validate the geometrical alignment between the RICH mirror system and the STRAW spectrometer, slopes measured by the STRAW are compared with slopes inferred from the RICH ring centre.

```
// Straw slopes
double slope_straw_x = pX / pZ;
double slope_straw_y = pY / pZ;

// RICH slopes
double slope_rich_x = RingCenterX / focal_length;
double slope_rich_y = RingCenterY / focal_length;

// Differences
double diff_x = slope_rich_x - slope_straw_x;
double diff_y = slope_rich_y - slope_straw_y;
```

The corresponding one– and two–dimensional distributions are used as cross–checks and are discussed in Chapter 4.

Bibliography

[1] P. A. Cherenkov. «Visible emission of clean liquids by action of gamma radiation». In: *Proceedings of the USSR Academy of Sciences* 2 (1934), pp. 451–454.

[2] I. M. Frank and I. E. Tamm. «Coherent visible radiation of fast electrons passing through matter». In: *Comptes Rendus de l'Académie des Sciences de l'URSS* 14 (1937), pp. 109–114.

[3] J. V. Jelley. *Cherenkov Radiation and its Applications*. Pergamon Press, 1958.

[4] W. R. Leo. *Techniques for Nuclear and Particle Physics Experiments*. Springer, 1994.

[5] NA62 Collaboration (E. Cortina Gil et al.) «The beam and detector of the NA62 experiment at CERN». In: *Journal of Instrumentation* 12 (2017), P05025. DOI: 10.1088/1748-0221/12/05/P05025.

[6] Ilaria Panichi. «Search for dark matter mediators in the rare decay$K^+ \to \mu^+\nu_\mu X$, with $X \to \gamma\gamma$. with the NA62 experiment at CERN». PhD thesis. Università di Firenze, 2020-21.